Helmer, E.H., Nicholas R. Goodwin, Valéry Gond, Carlos M. Souza Jr., and Gregory P. Asner. 2015. *Characterizing tropical forests with multispectral imagery.* Chapter 14, pages 367-396 *In* Prasad S. Thenkabail, Ed., Land Resources: Monitoring, Modeling and Mapping. Series: Remote Sensing Handbook. Taylor & Francis Group, Boca Raton, FL, USA. 849 p.

14

Characterizing Tropical Forests with Multispectral Imagery

E.H. Helmer
International Institute of Tropical Forestry, USDA Forest Service

Nicholas R. Goodwin
Ecosciences Precinct

Valéry Gond
Forest Ecosystems Goods and Services

Carlos M. Souza, Jr.
Instituto do Homen e Meio Ambiente da Amazônia

Gregory P. Asner
Carnegie Institution for Science

Acronyms and Definitions

AB-C	Aboveground live Biomass in units of Mg C ha^{-1}
ACCA	Automated Cloud Cover Assessment
AGLB	Aboveground Live Forest Biomass in Mg dry weight ha^{-1}
ASTER	Advanced Spaceborne Thermal Emission and Reflection Radiometer
AVHRR	Advanced Very High Resolution Radiometer
AWiFS	Advanced Wide Field Sensor
BRDF	Bidirectional Reflectance Distribution Function
BB-C	Belowground live Biomass in units of Mg C ha^{-1}
CBERS	China–Brazil Earth Resources Satellite
CDM	Clean Development Mechanism
DEM	Digital Elevation Model
DW-C	Dead Wood biomass in units of Mg C ha^{-1}
ESTARFM	Enhanced Spatial and Temporal Adaptive Reflectance Fusion Model
ETM+	Enhanced Thematic Mapper Plus
Fmask	Function of Mask
GHG	Greenhouse Gas
GLAS	Geoscience Laser Altimeter System
GV	Green Vegetation (unitless fraction, range 0–1)
HRG	High-Resolution Geometric
HRV	High-Resolution Visible
HRVIR	High-Resolution Visible and Infrared
HRS	High-Resolution Stereoscopic
IRMSS	Infrared Multispectral Camera
IRS	Indian Resources Satellite
INPE	Instituto Nacional de Pesquisas Espaciais
LI-C	Carbon content of forest floor litter in Mg C ha^{-1}
LISS	Linear Imaging Self-Scanner
MERIS	Medium-Resolution Imaging Spectrometer
MSS	Multispectral Scanner
MVC	Maximum-Value Compositing
NDFI	Normalized Difference Fraction Index (unitless, range –1 to 1)
NDMI	Normalized Difference Moisture Index

NPV	Non-Photosynthetic Vegetation (unitless fraction, range 0–1)
Mg	Megagram = 1×10^6 g = 1 metric ton
MAIAC	Multi-Angle Implementation of Atmospheric Correction for MODIS
MISR	Multi-angle Imaging SpectroRadiometer
MODIS	Moderate Resolution Imaging Spectroradiometer
MVC	Maximum-Value Compositing
NDVI	Normalized Difference Vegetation Index
NIR	Near-Infrared
SMA	Spectral Mixture Analysis
STARFM	Spatial and Temporal Adaptive Reflectance Fusion Model
REDD+	Reducing Emissions from Deforestation and Degradation, conservation of forest carbon stocks, sustainable management of forests, or enhancement of forest carbon stocks in developing countries
SO-C	Soil organic carbon in Mg C ha^{-1}
SPOT	Satellite Pour l'Observation de la Terre
SWIR	Shortwave Infrared
TM	Thematic Mapper
UNFCCC	United Nations Framework Convention on Climate Change
WiFS	Wide Field Sensor

14.1 Introduction

Tropical forests abound with regional and local endemic species and house at least half of the species on earth, while covering less than 7% of its land (Gentry, 1988; Wilson, 1988; as cited in Skole and Tucker, 1993). Their clearing, burning, draining, and harvesting can make slopes dangerously unstable, degrade water resources, change local climate, or release to the atmosphere the organic carbon (C) that they store in their biomass and soils as greenhouse gases (GHGs). These forest disturbances accounted for 19% or more of annual human-caused emissions of CO_2 to the atmosphere from the years 2000 to 2010, and that level is more than the global transportation sector, which accounted for 14% of these emissions. Forest regrowth from disturbances removes about half of the CO_2 emissions coming from the forest disturbances (Houghton, 2013; IPCC 2014). Another GHG of concern when considering tropical forests is N_2O released from forest fires.

Tropical forests (including subtropical forests) occur where hard frosts are absent at sea level (Holdridge, 1967), which means low latitudes, and where the dominant plants are trees, including palm trees, tall woody bamboos, and tree ferns. They include former agricultural or other lands that are now undergoing forest succession (Faber-Langendoen et al., 2012). They receive from <1000 mm $year^{-1}$ of precipitation to more than 10 times that much as rainfall or fog condensation. Whether dry or humid, tropical forests have far more species diversity than temperate or boreal forests, and their role in earth's atmospheric GHG budgets is large.

Multispectral satellite imagery, that is, remotely sensed imagery with discrete bands ranging from visible to shortwave infrared (SWIR) wavelengths, is the timeliest and most accessible remotely sensed data for monitoring these forests. Given this relevance, we summarize here how multispectral imagery can help characterize tropical forest attributes of widespread interest, particularly attributes that are relevant to GHG emission inventories and other forest C accounting: forest type, age, structure, and disturbance type or intensity; the storage, degradation, and accumulation of C in aboveground live tree biomass (AGLB, in Mg dry weight ha^{-1}); the feedbacks between tropical forest degradation and climate; and cloud screening and gap filling in imagery. In this chapter, the term *biomass* without further specification is referring to AGLB.

14.2 Multispectral Imagery and REDD+

14.2.1 Greenhouse Gas Inventories and Forest Carbon Offsets

Multispectral satellite imagery can provide crucial data to inventories of forest GHG sinks and sources. Inventories of GHGs that have forest components include national inventories for negotiations related to the United Nations Framework Convention on Climate Change (UNFCCC). The UNFCCC now includes a vision of compensating countries for reducing greenhouse gas emissions to the atmosphere from deforestation, degradation, sustainable management of forests, or conservation or enhancement of forest C stocks in developing countries (known as REDD+). Inventories of GHG emissions for the UNFCCC Clean Development Mechanism (CDM) may also include forests, and there are other forest carbon offset programs.

Programs like REDD+ could help moderate earth's climate. They could also help conserve tropical forests and raise local incomes, as long as countries make these latter goals a priority in REDD+ planning. Compensation in REDD+ is for organic carbon (C) stored in forest AGLB, dead wood, belowground live biomass, soil organic matter, or litter, as long as the stored C is "produced" by avoided GHG emissions, such as avoided deforestation or avoided degradation of forest C stores.

In forest C offsets, avoided emissions are estimated as the difference between net GHG emissions that would have occurred without implementing change (the *baseline case* or *business-as-usual scenario*) and actual net emissions that are reduced from what they would have been without the management change (the *project case*). Logging, burning, and fragmentation are examples of disturbances that degrade forest C stores. Replacing conventional logging with reduced impact logging reduces associated C emissions and is an example of avoided C emissions. For subnational projects such as those developed under voluntary carbon markets or the CDM, *leakage* must also be subtracted. *Leakage* refers net emissions that a carbon offset project displaces from its location to elsewhere. Examples are deforestation or removals of roundwood or fuelwood in a forest not far from the forest where such activities have ceased for forest C credits.

Many countries and organizations have officially proposed that forest C stored by enrichment planting, or by forest growth or regrowth on lands that were not forest before 1990, should also be explicitly eligible for REDD+ compensation (Parker et al., 2009). These latter activities, afforestation and reforestation, already dominate forest projects developed under the CDM.

14.2.2 Roles of Multispectral Imagery

The United Nations Intergovernmental Panel on Climate Change (IPCC) provides guidelines for GHG emission inventories, including for forest land (IPCC, 2006). Expanded methods based on these guidelines include those from the Verified Carbon Standard program (http://www.v-c-s.org). Summaries of these guidelines for communities seeking to certify carbon credits for voluntary carbon markets are also available (e.g., Vickers et al., 2012). For each stratum of each land use considered, changes in C stocks are estimated on an annual basis as the net of changes in the C pools as follows (in Mg C year^{-1}) (Equation 2.3, IPCC, 2006):

$$\Delta C_{LU} = \Delta C_{AB\text{-}C} + \Delta C_{BB\text{-}C} + \Delta C_{DW\text{-}C} + \Delta C_{LI\text{-}C} + \Delta C_{SO\text{-}C} + \Delta C_{HW\text{-}C} \quad (14.1)$$

where

ΔC_{LU} is the carbon stock changes for a land-use stratum, for example, a forest stratum, in Mg C year^{-1}

$\Delta C_{SUBSCRIPT}$ represents carbon stock changes for a given pool

Subscripts denote the following carbon pools in units of Mg C year^{-1}:

AB-C is the aboveground live biomass carbon

BG-C is the belowground biomass carbon

DW-C is the dead wood carbon

LI-C is the litter carbon

SO-C is the soil organic carbon

HW-C is the harvested wood carbon

For forest GHG inventories for REDD+ and other programs, multispectral satellite imagery can be used to estimate some of the key variables for Equation 14.1:

1. Areas of forest strata (e.g., forest types, disturbance/degradation classes, or management)
2. Baseline and ongoing rates of change in the areas of forest strata
3. The AGLB and rates of C accumulation in young forests
4. Point estimates of forest C pools in AGLB with fine-resolution imagery to supplement ground plot data
5. Potentially, forest AGLB if shown to be accurate for a given landscape
6. Potentially, GHG emission factors for forest disturbances if spectral indices of disturbance intensity can be calibrated to correlate well with associated GHG emissions and remaining C pools

Monitoring forest extent over large scales is also crucial to this forest C accounting, and multispectral satellite imagery is the best data for this purpose, but this topic is covered in other chapters of this book (Chapters 15, 17 through 19). Other chapters also cover multispectral image fusion with radar to map forest AGLB (e.g., Saatchi et al., 2011) or estimation of tropical forest biomass with airborne lidar (e.g., Asner et al., 2012). Multi-angular image data can also improve forest age mapping (Braswell et al., 2003).

When using the "stock-difference" method (IPCC, 2006) to quantify the parameters in Equation 14.1, the total C pool for each time period is estimated by multiplying the spatial density of C by the area (in hectare) of the forest stratum. The change in the C pool is estimated as the difference in C pools between two time periods divided by the elapsed time in years (please see Equation 2.5 in IPCC, 2006). In addition, in Equation 14.1, belowground biomass is usually estimated as a fraction of aboveground biomass with default values by ecological zone, region, or country. Also, when the type of land use is forest, litter can often be ignored.

The average spatial density of carbon in live biomass, in Mg C ha^{-1}, is estimated from the average spatial density of the dry weight of live biomass (in Mg ha^{-1}) multiplied by the C fraction of dry weight biomass. Typically, this C fraction is about 50% of dry weight mass. The IPCC (2006) has published default values for average C fraction of dry weight wood biomass by ecological zone. Dry weight is estimated with equations that relate the size of the trees growing in a forest to their dry weight, mainly as gauged by tree stem diameter and height. Then, the estimated dry weights of all trees in a known area are summed. Species-specific or regional equations are sometimes available.

14.3 Characteristics of Multispectral Image Types

Multispectral satellite imagery is available at spatial resolutions ranging from high (<5 m) to medium (5–100 m), to coarse (>100 m) (e.g., Table 14.1). The data usually include reflective bands covering the visible (blue, green, and red) and near-infrared (NIR) wavelengths of the electromagnetic spectrum. Several other sensors include SWIR bands (e.g., Landsat Thematic Mapper [TM] and subsequent Landsat sensors); the sensors aboard the fourth and fifth missions of Satellite Pour l'Observation de la Terre (SPOT 4 high-resolution visible and infrared [HRVIR], SPOT 5 high-resolution geometric [HRG], and the SPOT 4 and 5 Vegetation instruments); the Moderate Resolution Imaging Spectroradiometer (MODIS), the Advanced Wide Field Sensor (AWiFS), and the Infrared Multispectral Scanner Camera aboard the China–Brazil Earth Resources Satellite series [CBERS].

Satellite launches in the years 1998–1999 greatly increased the amount of imagery available for monitoring tropical forests. These launches brought (1) the first public source of high-spatial-resolution imagery (IKONOS, with <5-m pixels); (2) the first medium-resolution imagery (5–100 m pixels) with some degree of consistent global data collection (Landsat 7); (3) the first medium-resolution imagery with fine-resolution panchromatic bands of 2.5–5 m (SPOT 4 and Landsat 7, respectively);

TABLE 14.1 Multispectral Satellite Imagery Most Commonly Used to Characterize Tropical Forests

SatelliteRepeat/Revisit[a] Cycle, Scene Size/Swath Width Quantization	Band	Wavelength (μm)	Distributed Spatial Resolution (m)	Approximate Active Dates
High resolution (<5 m)				
IKONOS	Panchromatic	0.45–0.90	1	September 24, 1999 to present
3- to 5-day revisit	1-Blue	0.445–0.516	4	
11 × 11 km scenes	2-Green	0.506–0.595	4	
11 bits	3-Red	0.632–0.698	4	
	4-Near-infrared	0.757–0.853	4	
QuickBird	Panchromatic	0.45–0.90	0.6	October 18, 2001 to present
2- to 6-day revisit	1-Blue	0.45–0.52	2.4	
18 × 18 km Scenes	2-Green	0.52–0.60		
11 bits	3-Red	0.63–0.69		
	4-Near-infrared	0.76–0.90		
Medium resolution (5–100 m) with high-resolution panchromatic				
SPOT 4 HRVIR; SPOT 5 HRG	Panchromatic	0.51–0.73	2.5	SPOT 4: March 24, 1998 to July 2013
2–3 days Revisit	Panchromatic	0.51–0.73	5	SPOT 5: May 04, 2002 to present
60 × 60 km	Green	0.50–0.59	10	
8 bits	Red	0.61–0.68	10	
	Near-infrared	0.78–0.89	10	
	Shortwave infrared	1.58–1.75	20	
SPOT 1, 2, 3 HRV	Panchromatic	0.51–0.73	10	SPOT 1: February 22, 1986 to September 1990
1- to 3-day revisit	Green	0.50–0.59	20	SPOT 2: January 22, 1990 to July 16, 2009—
60 km × 60 km	Red	0.61–0.68	20	SPOT 3: September 26, 1993 to November 14, 1996
8 bits	Near-infrared	0.78–0.89	20	
Medium resolution (5–100 m)				
Landsat MSS 1,2,3 (4,5)	4 (1)-Blue–green	0.5–0.6	60[b]	Landsat 1: July 23, 1972 to January 06, 1978
16 days repeat	5 (2)-red	0.6–0.7	60[b]	Landsat 2: January 22, 1975 to February 25, 1982
170 × 185 km	6 (3)-Near-infrared	0.7–0.8	60[b]	Landsat 3: March 05, 1978 to March 31, 1983
4 bits	7 (4)-Near-infrared	0.8–1.1	60[b]	
Landsat 4 TM, 5 TM, 7 ETM+	1-Blue	0.45–0.52	30	Landsat 4: July 17, 1982 to December 14, 1993
16 days Repeat	2-Green	0.52–0.60	30	Landsat 5: March 1, 1984 to January 2013
170 × 183 km	3-Red	0.63–0.69	30	Landsat 7: April 15, 1999
8 bits	4-Near-infrared	0.76–0.90	30	
	5-Shortwave infrared	1.55–1.75	30	
	6-Thermal (2 ETM+ bands)	10.40–12.50	L4,5 120[c] (30) L7 60[c] (30)	
	7-Shortwave infrared	2.08–2.35	30	
	8-Panchromatic (L7 only)	0.52–0.90	15	
EO-1 ALI	MS-1'-Coastal aerosol	0.433–0.453	30	November 21, 2000 to present
16-day repeat	MS-1-Blue	0.45–0.515	30	
37 × 42 km	MS-2-Green	0.525–0.605	30	
12 bits	MS-3-Red	0.63–0.69	30	
	MS-4-Near-infrared	0.775–0.805	30	
	MS-4'-Near-infrared	0.845–0.89	30	
	MS-5'-Shortwave infrared	1.2–1.3	30	
	MS-5	1.55–1.75	30	
	MS-7	2.08–2.35	30	
	Panchromatic	0.48–0.69	10	

(*Continued*)

TABLE 14.1 (*Continued*) Multispectral Satellite Imagery Most Commonly Used to Characterize Tropical Forests

SatelliteRepeat/Revisit[a] Cycle, Scene Size/Swath Width Quantization	Band	Wavelength (μm)	Distributed Spatial Resolution (m)	Approximate Active Dates
Landsat 8	1-Coastal aerosol	0.433–0.453	30	February 11, 2013—
16-day repeat	2-Blue	0.450–0.515	30	
170 × 183 km	3-Green	0.525–0.600	30	
12 bits	4-Red	0.630–0.680	30	
	5-Near-infrared	0.845–0.885	30	
	6-SWIR 1	1.560–1.660	30	
	7-SWIR 2	2.100–2.300	30	
	8-Panchromatic	0.500–0.680	15	
	9-Cirrus	1.360–1.390	30	
	10-Thermal infrared 1	10.60–11.19	100[c] (30)	
	11-Thermal infrared 2	11.50–12.51	100[c] (30)	
Coarse resolution (>100 m)				
Terra/Aqua MODIS[d] (7 of 36 bands are shown)	1	0.620–0.670	250	Terra (EOS AM): August 12, 1999 to present
1-day revisit	2	0.841–0.876	250	Aqua (EOS PM): May 04, 2002 to present
2330 km Swath Width	3	0.459–0.479	500	
12 bits	4	0.545–0.565	500	
	5	1.230–1.250	500	
	6	1.628–1.652	500	
	7	2.105–2.155	500	
SPOT 4,5 Vegetation 1, 2[d]	0-Blue	0.43–0.47	1150	Aboard SPOT 4: March 24, 1998 to July 2013
1-day revisit	2-Red	0.61–0.68	1150	Aboard SPOT 5: May 04, 2002 to present
2250 km Swath Width	3-Near-infrared	0.78–0.89	1150	
10 bits	SWIR-Shortwave infrared	1.58–1.75	1150	

[a] Revisit cycles change with latitude.
[b] The original MSS pixel size of 79 × 57 m is now resampled to 60 m.
[c] Thermal infrared Landsat bands are now resampled to 30 m.
[d] For coarse-resolution sensors, resolution given is at nadir.

and (4) the first coarse-resolution imagery (>100 m pixels) distributed with higher-level preprocessing like atmospheric correction and cloud-minimized compositing (MODIS and SPOT Vegetation). Before IKONOS, remotely sensed reference data had to come from air photos that in many places were costly to obtain and outdated.

The next big advances in tropical forest monitoring with satellite imagery came in 2005–2008, when (1) Google, Inc. and the producers of high-resolution imagery such as QuickBird and IKONOS made high-resolution data viewable on Google Earth for many sites, making reference data free and accessible for subsets of project areas; and (2) the Brazilian National Institute for Space Research (INPE) and the United States Geological Survey (USGS) began to freely distribute Landsat and other imagery with medium spatial resolution, making long, dense time series of medium-resolution imagery available over large areas.

Other sources of multispectral imagery for monitoring tropical forests over large areas that are not shown in Table 14.1, mainly to highlight them here, include the Japan–U.S. Advanced Spaceborne Thermal Emission and Reflection Radiometer (ASTER) (aboard Terra). In addition to 15 m VNIR bands, it has several SWIR and thermal bands with 30–90 m spatial resolution. Data for Brazil and China and nearby areas are also available from CBERS. The series of CBERS satellites, 1, 2, and 2B, collected panchromatic to SWIR images with medium spatial resolution (20–80 m, 113–120 km swath width), and red and NIR images with coarse spatial resolution (260 m, 890 km swath width) from 1999 to 2010 and missions to collect with medium-resolution multispectral imagery with a 5-day revisit cycle are scheduled. In the Indian Resources Satellite (IRS) series, the Wide Field Sensor (WiFS) has a 740 km swath width, 188 m spatial resolution, and red and NIR bands. More recently, the IRS-P6 satellite carries the AWiFS instrument. AWiFS has 60 m pixels for green through SWIR bands, a 740 km swath width, a 5-day revisit cycle, and a SWIR band, combining advantages of imagery with medium and coarse spatial resolutions. The later of the IRS series sensors include data from Linear Imaging Self-Scanner (LISS) with multispectral imagery with a 23.5 m spatial resolution. Ground stations receiving data from CBERS and the IRS satellite series have not covered all of the tropics. Fortunately, that situation should gradually change.

14.4 Preprocessing Imagery to Address Clouds

14.4.1 Cloud Screening

We begin with cloud and cloud shadow screening, as this step is crucial in the image processing chain for characterizing tropical forests. Clouds and their shadows obscure the ground and contaminate temporal trends in reflectance. Automated systems for processing large archives of satellite imagery are becoming more common for natural resource applications and must screen clouds. Clouds are composed of condensed water vapor that form water droplets and scatter visible to NIR light, reducing direct illumination on the surface below and forming a cloud shadow. In multispectral satellite imagery, clouds are characterized by a high albedo (Choi and Bindschadler, 2004), while their shadows have lower reflectance than surrounding pixels. The easiest solution to cloud contamination is to restrict analyses to cloud-free imagery, which may include only dry season imagery for tropical and coastal environments due to frequent cloud cover. Alternatively, methods to screen cloud- and shadow-contaminated pixels can increase the number of observations available (Figure 14.1). Increasing the number of available observations in a time series may also improve the detection of land surface change and reflectance trends.

Manual and semiautomated approaches to cloud screening are undesirable for processing large numbers of images due to the time-consuming nature of the work, which may depend not only on analyst experience but also on image contrast. Several automated approaches have been developed, but separating cloud and shadow from the land surface is not necessarily straightforward given the diversity of land surfaces coupled with large variations in cloud and shadow optical properties (Lyapustin et al., 2008; Zhu et al., 2012; Goodwin et al., 2013). AQ4
A summary of current approaches to cloud and shadow screening for Landsat TM/ETM+, SPOT, and MODIS sensors follows.

14.4.1.1 Landsat TM Imagery

The Landsat TM/ETM+ archives of countries with receiving stations now contain up to three decades of imagery (1984 to present) with varying levels of cloud and cloud shadow contained in the archive of images. The U.S. Geological Survey is working with other countries to consolidate these archives through consistent processing and distribution through its website (landsat.usgs.gov). Image preprocessing by the Landsat program has included the Automatic Cloud Cover Assessment (ACCA) algorithms for both Landsat-5 TM and Landsat-7 ETM+ missions, which use optical and thermal (ETM+ only) bands to identify clouds (Irish, 2006). It is designed for reporting the percentage of cloud cover over scenes rather than producing per-pixel masks. Further modifications have also been tested for application to Landsat 8 imagery (Scaramuzza et al., 2012), which includes a AQ5
new cirrus band (1.360–1.390 μm) that is sensitive to aerosol loadings and should improve cloud detection. ACCA is designed to limit the impacts of cloud and scene variability on thresholding. The ETM+ ACCA incorporates two passes: one to conservatively estimate "certain" cloud at the pixel level with a series of spectral and thermal tests. The result is then used to derive scene-based thermal thresholds for the second pass. The error in scene-averaged cloud amount was estimated to be around 5% (Irish et al., 2006). Scaramuzza et al. (2012) validated the

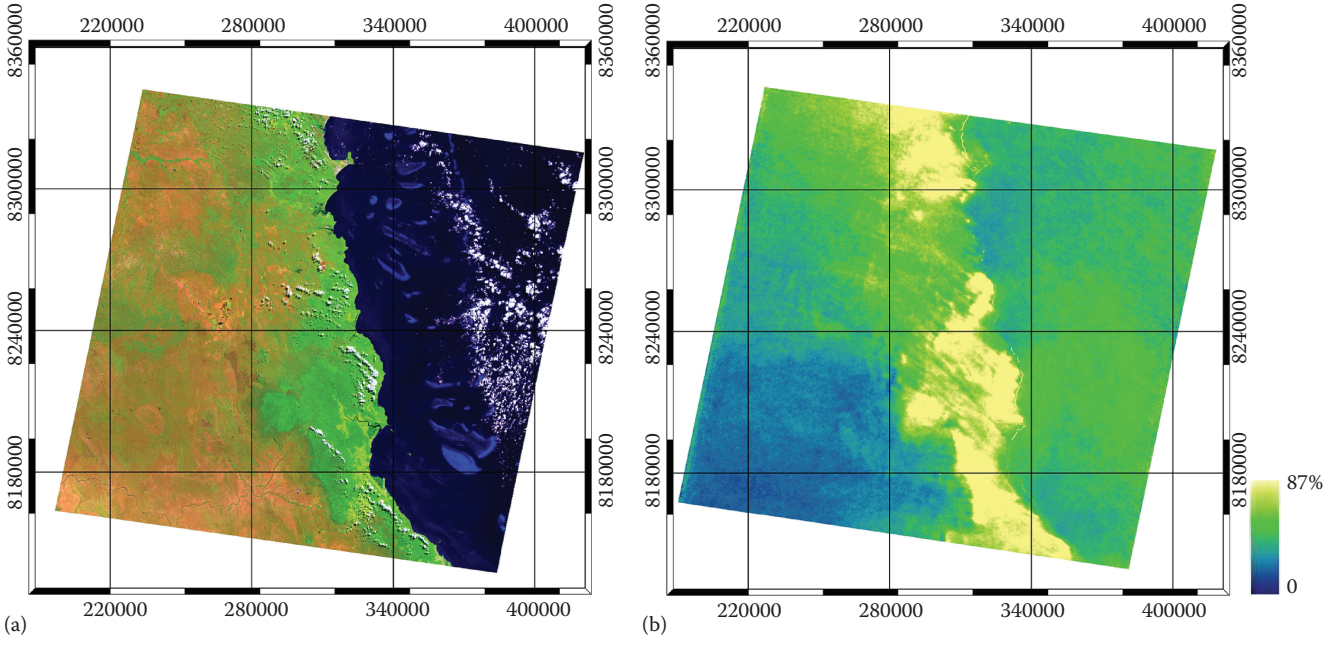

FIGURE 14.1 Illustration of cloud distribution spatially and temporally over tropical forests of north Queensland: (a) Landsat image (RGB: 542, Path/Row: 96/71, and date July 02, 2007) and (b) percentage of observations classified as cloud between 1986 and 2012 (n = 445). Note: high cloud fractions were not included in calculations.

per-pixel classification of the ETM+ ACCA (pass 1) and found a 79.9% agreement between reference and ACCA at the pixel scale. Using a subset of the same reference set, Oreopoulos et al. (2011) evaluated both per-pixel ACCA masks and a cloud detection algorithm modified from the MODIS Luo–Trishchenko–Khlopenkov algorithm (Luo et al., 2008). Both ACCA and the modified LTK showed greater than 90% agreement with the reference, although like ACCA, the LTK had limited ability to detect thin cirrus clouds. Furthermore, ACCA has been used as the starting point for further cloud masking (Choi and Bindshadler, 2004; Roy et al., 2010; Scaramuzza et al., 2012).

Earlier studies have shown that several approaches work well for classifying clouds and cloud shadows over particular path/rows. One approach is image differencing based on image pairs (Wang, 1999), while other studies have empirically defined thresholds for cloud brightness and coldness in one or more spectral/thermal bands, for example, Landsat TM Bands 1 and 6 (Martinuzzi et al., 2007); Bands 3 and 6 (Huang et al., 2010); Bands 1, 3, 4, and 5 (Oreopoulos et al., 2011); and Bands 1, 4, 5, and 6 (Helmer et al., 2012). The application of these methods to a range of path/rows around the globe, however, remains untested and may encounter issues due to spectral similarities among the wide range of combinations of land surfaces and cloud/cloud shadows.

The automated method that Huang et al. (2010) developed to allow forest change detection in cloud-contaminated imagery considers brightness and temperature thresholds for clouds that are self-calibrated against forest pixels. It requires a digital elevation model to normalize top of atmosphere brightness temperature values and helps to project cloud shadow on the land surface. Published validation data for this method are currently limited to four U.S. images with forest and would benefit from further calibration/validation.

Two additional automated approaches have recently been published: Fmask (Function of mask) (Zhu and Woodcock, 2012) and a time series approach by Goodwin et al. (2013) (Figure 14.2). Fmask integrates existing algorithms and metrics with optical and thermal bands to separate contaminated pixels from land surface pixels. Fmask also considers contextual information for mapping potential cloud shadow using a flood-fill operation applied to the NIR band. Cloud shadows are then identified by linking clouds with their shadow with solar/sensor geometry and cloud height inferred from the thermal Landsat TM Band 6. The results were validated with a global dataset and were a significant improvement to ACCA with Fmask achieving an overall, user's, and producer's accuracies of 96%, 89%, and 92%, respectively compared to 85%, 92%, and 72%, respectively for ACCA.

The time series method uses temporal change to detect cloud and cloud shadow (Goodwin et al. (2013)). It smoothes pixel time series of land surface reflectance using minimum and median filters and then locates outliers with multi-temporal image differencing. Seeded region grow is applied to the difference layer using a watershed region grow algorithm to map clusters of change pixels, with clumps smaller than 5 pixels removed to minimize classification speckle. This has the effect of increasing the cloud/shadow detection rate while restricting commission errors; smaller magnitudes of change associated with cloud/cloud shadows are mapped only if they are in the neighborhood of larger changes. Morphological dilation operations were applied to map a larger spatial extent of the cloud and cloud shadow, while shadows were translated along the image plane in the reverse solar azimuth direction to assess the overlap with clouds and confirm the object is a shadow. A comparison with Fmask showed that the time series method could screen more cloud and cloud shadow than Fmask across Queensland, Australia (cloud and cloud shadow producer's accuracies were 8% and 12% points higher, respectively).

Several trade-offs exist between these two automated approaches to cloud and shadow screening. The time series method might detect more cloud and cloud shadow, yet Fmask is more computationally efficient and practical for individual images. At present, the time series method is processed using entire time series for each Landsat path/row. For operational systems processing many images, the computational overhead of the time series approach could be worthwhile as it can detect more cloud/shadow contamination. Locations with few cloud-free observations per year and high land-use change are also less desirable for a time series method. In the absence of an atmospheric aerosol correction, pixels contaminated by smoke and haze are more likely to be classified as cloud by the time series method. Neither the Fmask nor the time series method nor previous attempts adequately map high level, semitransparent cirrus cloud (Figure 14.2d–f). New methods for Landsat 8 will likely detect more cloud with the new band sensitive to cirrus clouds. Both Fmask and the time series methods are highly configurable allowing calibration for a localized region or a wider application. Fmask has been calibrated using a global reference set, while the time series approach was calibrated and tested mainly for northeastern Australian conditions.

Although both methods have high accuracy, further improvements could be made particularly to screening cloud shadow. Removing the dependency of a link between cloud and shadow would be a considerable advancement as clouds are often missed or under/overmapped, causing the shadow test to fail. Furthermore, adding thermal information to the time series method has the potential to remove commission errors where bright surfaces such as exposed soil are falsely classified as cloud. Both methods use a series of rules to classify cloud and shadow and have the flexibility to add new algorithms and criteria to improve the detection of contaminated pixels.

14.4.1.2 SPOT Imagery

The spatial and spectral characteristics of SPOT (Satellite Pour l'Observation de la Terre) have similarities to Landsat imagery, with the first satellite launched in 1986 (SPOT 1), and similar methods for screening cloud and cloud shadows should be useful. The main exception is that SPOT lacks a thermal band, which has been useful in discriminating clouds (e.g., ACCA). However, only a limited number of studies have been published

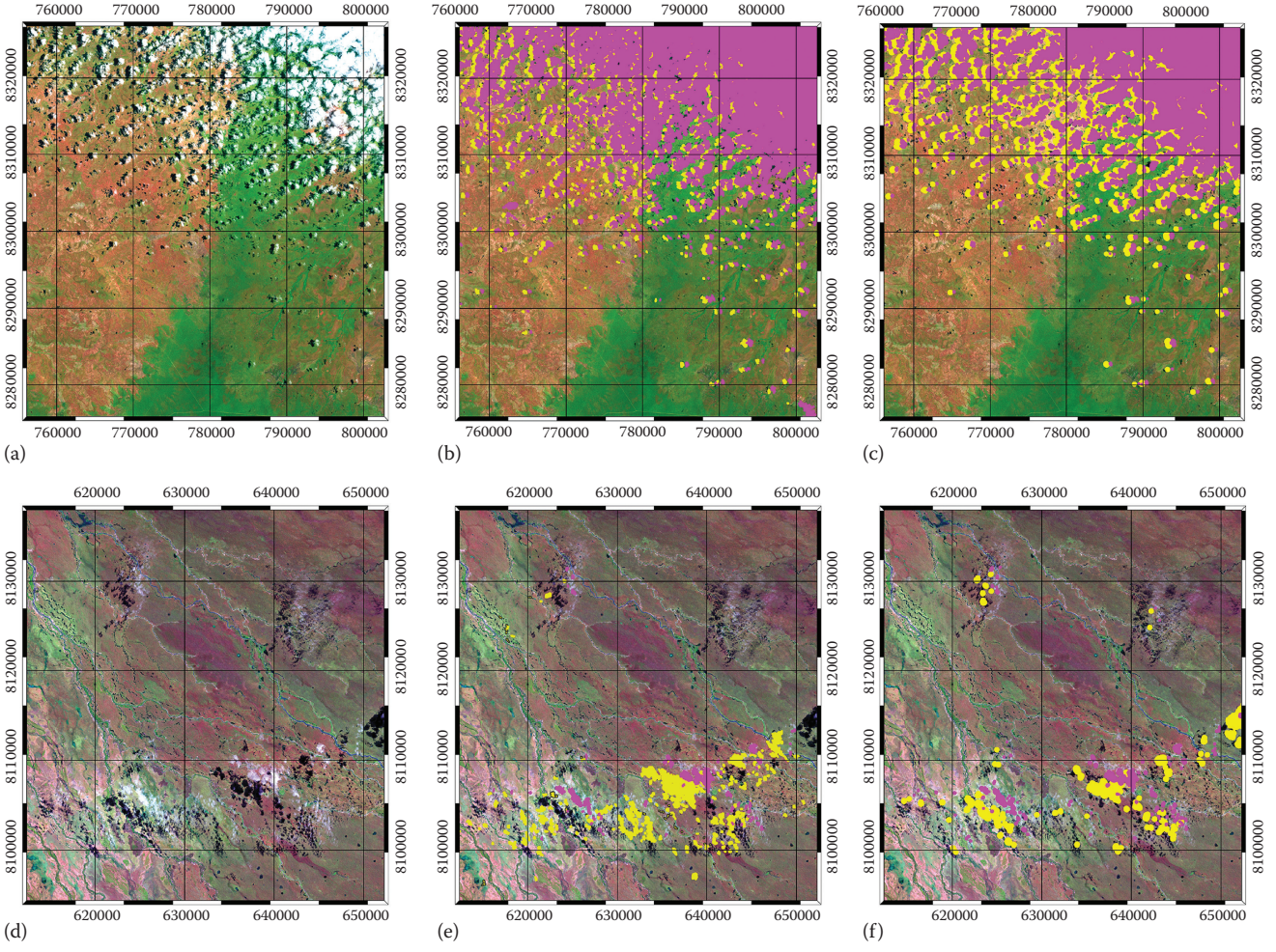

FIGURE 14.2 Examples of Fmask and time series approaches to cloud and cloud shadow screening: (a) Landsat TM image, (b) TS classification, (c) Fmask classification, (d) Landsat TM image, (e) TS classification, and (f) Fmask classification, (a–c) well-detected cumulus cloud and cloud shadow (RGB: 542, Path/Row: 97/71, and date October 10, 1998) and (d–f) a complex example where both methods miss sections of cirrus cloud (RGB: 542, Path/Row: 98/72, and date April 04, 2001).

on screening cloud and cloud shadow from SPOT data. SPOT is a commercially operated sensor, and unlike Landsat TM/ETM+ and MODIS, scenes are typically purchased/tasked with limited cloud cover or would otherwise prove cost prohibitive for many vegetation applications. The New South Wales government of Australia, for example, acquired 1850 images between 2004 and 2012, of which only 313 contain cloud with the maximum cloud cover values <10% (Fisher, 2014).

Le Hégarat-Mascle and André (2009) used a Markov random field framework that assumes that clouds are connected objects, solar/sensor geometry is known, and shadow has a similar shape to its corresponding cloud (excluding the influence of topography). Potential cloud pixels were identified using a relationship between green and SWIR bands; shadows were located using cloud shape, orientation of shadow relative to cloud and SWIR band reflectance, removing objects not part of a cloud–shadow pair. The method was applied to 39 SPOT 4 HRVIR images over West Africa with encouraging results. However, when applying this method, Fisher (2014) found commission errors as bright surfaces were frequently matched to dark surfaces that were not cloud contaminated. They suggest first masking vegetation and water bodies, then locating marker pixels for clouds and shadows in the green–SWIR space and NIR bands, respectively, then growing objects with the watershed transform. Sensor/solar geometry and object size are also used to match clouds with their shadows.

14.4.1.3 MODIS Imagery

MODIS has a standard cloud product, in contrast to SPOT or until recently Landsat, which includes information on whether a pixel is clear from cloud/shadow contamination. The cloud mask is based on several per-pixel spectral tests and is produced at 250 m and 1 km spatial resolutions (Strabala, 2005). A validation with active ground-based lidar/radar sensors showed an 85% agreement with the MODIS cloud mask (Ackerman et al., 2008).

Recent research has found that time series information can improve cloud detection in MODIS imagery (Lyapustin et al., 2008; Hilker et al., 2012). The cloud-screening method

in multi-angle implementation of atmospheric correction, for example, uses a dynamic clear-sky reference image and covariance calculations, in addition to spectral and thermal tests, to locate clouds over land (Lyapustin et al., 2008). In a tropical Amazonian environment, Hilker et al., 2012 demonstrated that this method was better at detecting clouds and increasing the number of usable pixels than the standard product (MYD09GA), which translated into more accurate patterns in NDVI.

14.4.2 Filling Cloud and Scan-Line Gaps

Cloud and cloud shadow screening removes contaminated pixels from analyses but leaves missing data in the imagery and derived products. The scan-line correction error affecting Landsat 7 post-2003 also leaves gaps approximating 20% of affected images (USGS, 2003). Data gaps in maps are aesthetically unappealing, and the derivation of statistics is more difficult. As a result, approaches have been developed to fill data gaps including temporal compositing and fusing imagery from two different sensors.

A range of temporal compositing algorithms have been developed to minimize cloud contamination and noise (Dennison et al., 2007; Flood, 2013). Compositing involves analyzing band/metric values across a date range with an algorithm deciding the pixel value most likely to be cloud/noise free. The choice of algorithm may vary depending on the application and land-cover type. Compositing algorithms have generally been applied to high-temporal-frequency data such as MODIS and AVHRR; however, methods for compositing imagery with a lower temporal resolution have also been developed. For example, the MOD 13 products use the maximum-value compositing algorithm with NDVI as the metric in 16-day and monthly composites of MODIS imagery (Strabala, 2005). Landsat has similarly been composited using a parametric weighting scheme (Griffiths et al., 2013). The result is an image that ideally is free from noise or cloud that can be used as a product itself or the corresponding pixels used to infill data gaps.

The fusion or blending of MODIS and Landsat offers another approach to predict image pixel values within data gaps. These methods integrate medium-spatial-resolution Landsat with temporal trends in reflectance (e.g., seasonality) captured by the higher temporal frequency of MODIS. Roy et al. (2008) integrated the MODIS bidirectional reflectance distribution function (BRDF)/albedo product and Landsat data to model Landsat reflectance. They found that infrared bands were more accurately predicted than visible wavelengths, probably in response to greater atmospheric effects at shorter wavelengths. The spatial and temporal adaptive reflectance fusion model (STARFM) requires a MODIS–Landsat image pair captured on the same day plus a MODIS image on the prediction date and applies spatial weighting to account for reflectance outliers (Gao et al., 2006). Further algorithm development has produced an enhanced STARFM (ESTARFM) method that was found to improve predictions in heterogeneous landscapes (Zhu et al., 2010). However, there are known limitations with blending or fusing Landsat and MODIS imagery. Solutions involving MODIS will work only post-2000 when imagery was first captured and potentially 2002 onward where stable BRDF predictions are needed (Roy et al., 2008). Furthermore, Emelyanova et al. (2013) found that land-cover type and temporal and spatial variances impact the fusion of MODIS and Landsat as well as the choice of algorithm. Where the temporal variance of MODIS is considerably less than the spatial variance of Landsat, blending may not improve predictions.

Gap filling using Landsat imagery alone has also been performed. Helmer and Ruefenacht (2005) developed a method for predicting Landsat values using two Landsat images for change detection. This method develops a relationship between uncontaminated pixels in an image pair with regression tree models, and it then applies these models to predict the values in areas with missing data in the target image. Additional images are used in the same way to predict pixels in remaining cloud gaps. Langner et al. (2014) segment such pairwise predictive models according to forest type. Approaches using geostatistics have also been developed. Pringle et al. (2009) use an image before and after the target image in geostatistical interpolation to predict values in Landsat 7 SLC-off imagery. Based on their results, they recommend images captured within weeks, rather than months, of each other to limit temporal variance in a tropical savanna environment. Zhu et al. (2012) also use geostatistics with encouraging results to predict missing Landsat 7 SLC-off data based on the Geostatistical Neighborhood Similar Pixel Interpolator.

A potential limitation with gap filling is the introduction of image noise or artifacts. This is because of differences in vegetation phenology, illumination, and atmospheric effects as gap-filled imagery contains data from multiple dates and/or sensors. These effects can be minimized by atmospheric and illumination corrections as well as methods that seek to balance the distribution of pixel values such as histogram matching, linear regression, or regression trees (Helmer and Ruefenacht, 2007). AQ6

14.5 Forest Biomass, Degradation, and Regrowth Rates from Multispectral Imagery

Studies have used multispectral imagery to map or estimate some key inputs to the variables in Equation 14.1 (Section 14.2.2) for forests: forest AGLB (in Mg dry weight ha^{-1}), rates of C accumulation in reforesting lands (in Mg dry weight ha^{-1} $year^{-1}$), and area or intensity of forest degradation or disturbance (in ha). In addition, multispectral imagery is the most common satellite imagery for mapping tropical forest types, which we discuss in Section 14.6, and AGLB estimates are often more precise and accurate if stratified by forest type.

In this section, we first review work that uses the spectral and textural information in multispectral imagery of high spatial resolution to estimate tropical forest AGLB. We then discuss how the spectral information inherent to multiyear image time

series has high sensitivity to the height, AGLB, and age of forests that have established since about 10 years before the start of an image sequence (so as early as 10 years before 1972 for Landsat data), which we refer to here as *young forests*, allowing estimates of biomass and C accumulation rates in reforested lands. Next, we discuss how multispectral imagery from a single epoch of medium- to coarse-spatial-resolution imagery has limited sensitivity to tropical forest age or biomass. Section 14.5.3 focuses on detecting tropical forest degradation at pixel and subpixel scales.

14.5.1 Tropical Forest Biomass from High-Resolution Multispectral Imagery

When considering forest structure mapping, multispectral imagery of high spatial resolution, with pixels ≤5 m, is distinct from imagery with medium spatial resolution because the spatial patterns of dominant and codominant tree crowns are visible. The possibility of detecting tree crown size suggests a way to estimate AGLB by allometry between stem diameters, used to estimate AGLB, and crown size (Asner et al., 2002; Couteron et al., 2005; Palace et al., 2008). Automated crown delineation in these images is more accurate than manual means, but both methods overestimate the area of large crowns and underestimate the frequency of understory and codominant trees (Asner et al., 2002; Palace et al., 2008), such that biomass estimates from crown delineation alone require adjustments.

A new technique, however, predicts the biomass of high-biomass tropical forests with stand-level spatial patterns of tree crowns in images with ~1 m or finer pixels. The new method first applies two-dimensional Fourier transforms to subsets (*samples*) of high-resolution panchromatic images, from which it produces a dataset with a row for each sample of imagery and columns that bin the outputs from the transform so that the columns in each row together form a proxy for the distribution of crown sizes discerned or "apparent" in each image sample. Principal components transformation of this matrix yields axes that serve as predictors in regression models of stand structural parameters, like basal area, AGLB, or "apparent" dominant crown size (calculated by inversion) (Couteron et al., 2005; Barbier et al., 2010; Ploton et al., 2011). Ploton et al. (2011) predicted forest biomass ranging from ~100 to over 600 Mg ha^{-1} in Western Ghats, India, with IKONOS image extracts downloaded from Google Earth Pro (0.6–0.7 m resolution). Their model explained 75% of the variability in forest biomass. They estimated that the relative uncertainty in AGLB estimates that was due to the remote sensing technique, of <15%, was similar to uncertainties associated with estimating forest AGLB with lidar. With this new technique, AGLB estimates from high-resolution imagery on Google Earth could supplement ground- or lidar-based surveys. The resulting increase in the number and density of AGLB estimates for forests should better characterize the landscape-scale spatial variability in AGLB and increase the precision of forest C-pool estimates.

Related to the earlier work on AGLB are studies that have characterized how gradients in the spatial patterns of tropical forest canopies correspond with climate. These gradients are apparent in high-resolution imagery, and future changes in these patterns could reflect and help monitor effects of global climate change (Malhi and Román-Cuesta, 2008; Palace et al., 2008; Barbier et al., 2010). Barbier et al. (2010), for example, showed how dominant crown size and canopy size heterogeneity change with climate and substrate across Amazonia.

14.5.2 Biomass, Age, and Rates of Biomass Accumulation in Forest Regrowth

With a long time series of medium-resolution multispectral images such as Landsat, key variables for GHG inventories (and forest C accounting for REDD+) can be mapped and estimated for young tropical forests, including area, age, height, AGLB, and rates of biomass accumulation. Where an image time series spans the age range of young forests, its spectral data can precisely estimate age, which is needed to estimate biomass accumulation rates and can also help estimate the height or AGLB of these forests. Helmer et al. (2009) estimated a landscape-level rate of AGLB accumulation in Amazonian secondary forest by regressing forest biomass estimates from the Geoscience Laser Altimeter System (Figure 14.3) against remotely sensed forest age (R-square = 0.60). The estimated landscape-level biomass accumulation rate of 8.4 Mg ha^{-1} year^{-1} agreed well with ground-based studies. Forest age was mapped with an algorithm that automatically processed a time series of Landsat MSS and TM imagery (1975–2003) with self-calibrated thresholds that detect

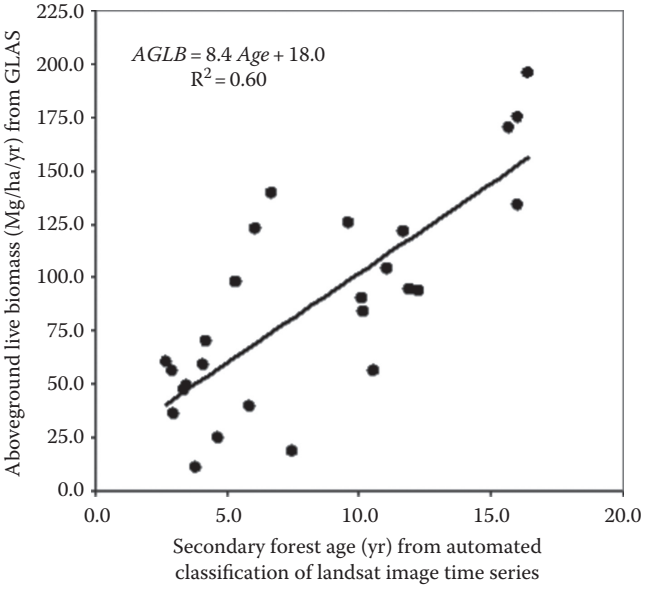

FIGURE 14.3 The average age of secondary forest pixels, as estimated from automatic processing of a time series of Landsat MSS, TM, and ETM+ imagery, in the 150 m window surrounding GLAS waveform centers explained 60% of the variance in GLAS-estimated canopy height and biomass (aboveground live biomass, AGLB, in Mg ha^{-1} year^{-1} dry weight). The standard error of the slope and intercept are 1.4 and 13.2, respectively, for 26 observations. AQ7

when secondary forests established on previously cleared land. The technique mapped the extent of old-growth forest and age of secondary forest with an overall accuracy of 88%. With the time series, tropical secondary forest >28 years old was accurately distinguished from old-growth forest, even though it was spectrally indistinct in the most recent Landsat scenes. This older secondary forest clearly stored less C than the old-growth forest, being shorter and having much smaller average canopy diameters than nearby old growth.

Forest height and AGLB are strongly related, and the height or AGLB of young forests can be mapped with long time series of Landsat images in tropical (Helmer et al., 2010) and temperate (Li et al., 2011; Plugmacher et al., 2012; Ahmed et al., 2014) regions. With a regression tree model based on the spectral data from all of the images in a time series of cloud-gap-filled Landsat imagery (1984–2005 with 1- to 5-year intervals), Helmer et al. (2010) mapped the height (RMSE = 0.9 m, R-square = 0.84, range 0.6–7 m) and foliage height profiles of tropical semievergreen forest (Figure 14.4). In contrast with mapping the height of old forests, local-scale spatial variability in young forest structure was mapped, because within-patch differences in disturbance intensity and type, and subsequent forest recovery rate, were reflected in the spectral data from the multiyear image stack. This study also mapped forest disturbance type, age, and wetland forest type, with an overall accuracy of 88%, with a decision tree model of the entire time series of cloud-minimized composite images to better understand avian habitat. As a result, the classification distinguished different agents of forest disturbance, including classes of cleared forests and forests affected by escaped fire, and allowed estimation of rates of forest regrowth. Forest age, vertical structure, and disturbance type explained differences in woody species composition, including abundance of forage species for an endangered Neotropical migrant bird, Kirtland's warbler *Dendroica kirtlandii*.

14.5.3 Limitations to Mapping Forest Biomass or Age with One Multispectral Image Epoch

14.5.3.1 Tropical Forest Biomass with One Image Epoch

Forest biomass mapping with multispectral imagery empirically predicts the AGLB of forested pixels with models that relate forest AGLB or height, from ground plots or lidar, to spectral bands, spectral indices, or spectral texture variables. It remains a challenge (Song, 2013). Forest AGLB is usually estimated in units of Mg dry weight ha^{-1} (see Section 14.2). As more data on stand species composition and species-specific wood densities become available, maps of C storage in forest biomass, as in Asner et al. (2013) and Michard et al. (2014), rather than forest biomass itself, may become more common.

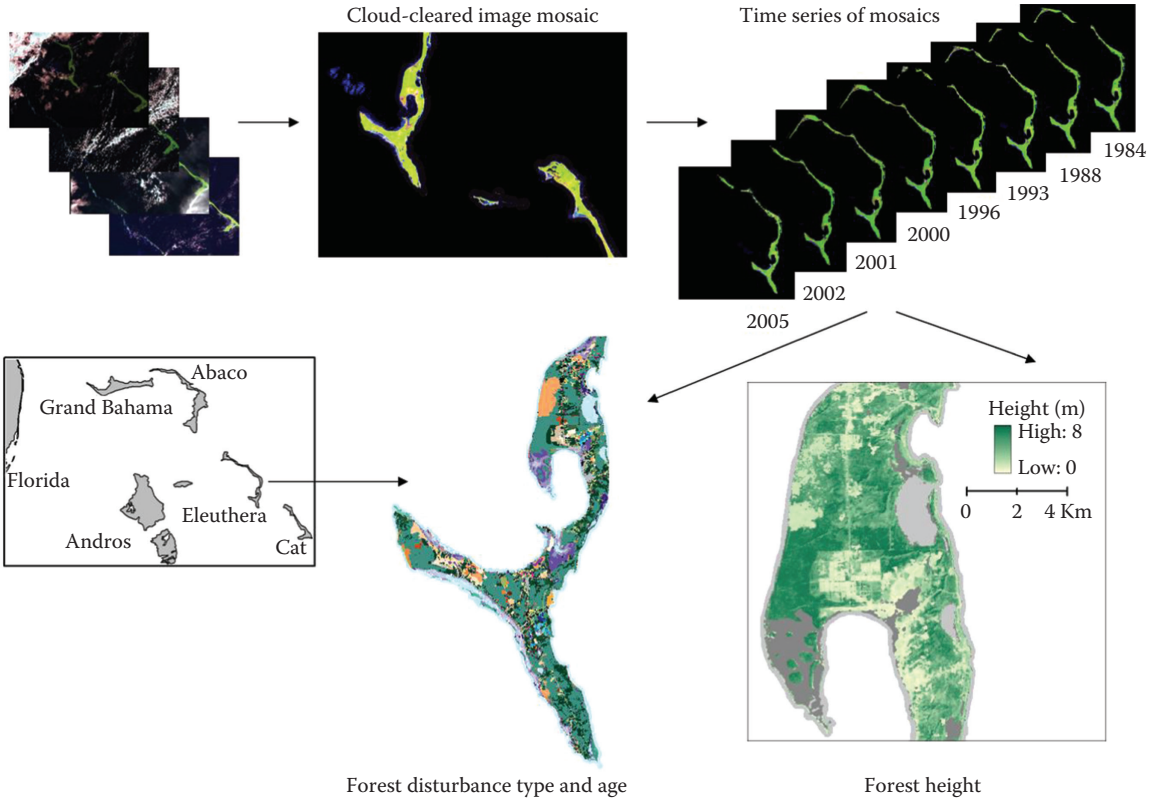

FIGURE 14.4 Tropical dry forest height and foliage height profiles were mapped from a time series of gap-filled Landsat and ALI imagery on the island of Eleuthera, The Bahamas, substituting time for vertical canopy space. The time series was also used to map forest disturbance type and age.

Medium- to coarse-spatial-resolution imagery from one epoch is not that sensitive to small changes in the AGLB or C storage in aboveground biomass of dense tropical forests. (By *epoch*, we mean imagery from one date, one gap-filled, or composite image composed of imagery from one to several years, or multiseason imagery from 1 year.) This limited sensitivity appears in biomass mapping models as high per pixel uncertainty that can manifest itself in several ways:

1. Mapping models may explain a minority of variance in reference data (i.e., regressions of predicted vs. observed values have low coefficients of determination or R-squared values of less than 0.50) (e.g., Oza et al., 1996 for volume of Indian deciduous forest; Steininger, 2000 for Bolivian sites; Wijaya et al., 2010 in Indonesia).
2. Mapping models may both underestimate AGLB at high-biomass sites and overestimate AGLB where biomass is low (e.g., Baccini et al., 2008 for tropical Africa; Blackard et al., 2008 for the United States including Puerto Rico; Wijaya et al., 2010).
3. Spectral responses to AGLB may saturate at relatively low levels of around 175 Mg C ha^{-1}. For example, studies indicate that stand-level multispectral responses saturate at 150–170 Mg ha^{-1} for study sites in Brazilian Amazonia (Steininger, 2000; Lu, 2005), ~180 Mg C ha^{-1} in Panama (Asner et al., 2013), and 175 Mg ha^{-1} across Uganda (Avitabile et al., 2012). These saturation levels may be half or less of the biomass of the most structurally complex or old-growth tropical forests in humid lowlands. In many landscapes, the relationship between multispectral data and tropical forest AGLB may saturate at even lower levels.
4. Continental- to global-scale mapping models may not capture gradients in AGLB and C pools that stem from differences in forest allometry and average wood density (Mitchard et al. (2014).

Despite per-pixel uncertainties, estimates of the total forest biomass may be accurate when pixels are summed over large areas that have a wide range of AGLB. This result could happen when the average biomass of pixels covering a large area approaches the mean of the ground or lidar data used to estimate the mapping model. Estimates of total forest AGLB across tropical landscapes can also be accurate if the landscapes that have few forest patches with AGLB exceeds the levels where spectral response becomes saturated (e.g., Avitabile et al. 2012).

Texture variables from SPOT 5 imagery may improve mapping models of AGLB, because SPOT 5 imagery has finer spatial resolutions of 10–20 m compared with many other image sources with medium spatial resolution (Table 14.1), but results may still have relative errors of around 20% (Castillo-Santiago et al., 2010). Exceptions may include Asian bamboo forests (Xu et al., 2011) or low-biomass tropical forests.

Mapping models of tropical forest AGLB or height that rely on multispectral imagery benefit from added predictors. Example predictors that may improve models include topography, forest type, climate, soils, geology, or indicators of disturbance like tree canopy cover (Helmer and Lefsky, 2006; Saatchi et al., 2007; Blackard et al., 2008; Asner et al., 2009; Lefsky, 2010; Wijaya et al., 2010). After including these predictors in mapping models, the variability in the biomass mapped for undisturbed forests may reflect more of the variability in AGLB that stems from regional- to landscape-scale environmental gradients in attributes like rainfall. Maps of these spatial patterns may be useful, but they may not reveal much local-scale AGLB variation.

14.5.3.2 Tropical Forest Age with One Image Epoch

As with AGLB, multispectral imagery has limited sensitivity to increasing forest age. Many studies show that spectral indices that contrast the mid-infrared bands with the near-infrared or visible bands are the most sensitive indices to tropical forest age, height, and AGLB (e.g., Boyd et al., 1996; Helmer et al., 2000; Steininger, 2000; Thenkabail et al., 2003; Helmer et al., 2010). For example, with Landsat TM or ETM+ data, these indices include the NIR/SWIR ratio, the tasseled cap wetness index (Crist and Cicone, 1984; Huang et al., 2002), the wetness brightness difference index (WBDI) (Helmer et al., 2009), and the normalized difference moisture index (NDMI) (also referred to as the normalized difference structure index and the normalized difference infrared index). The WBDI and NDMI are calculated as

$$\text{WBDI} = \text{TC Wetness} - \text{TC Brightness} \tag{14.2}$$

$$\text{NDMI} = \frac{(\text{NIR}_{b4} - \text{SWIR}_{b5})}{(\text{NIR}_{b4} + \text{SWIR}_{b5})} \tag{14.3}$$

However, lowland humid tropical forests recovering from previous clearing may become spectrally indistinct from mature forests within 15–20 years (Boyd et al., 1996; Steininger, 2000), though slower-growing tropical forests, like montane or dry forests, can remain spectrally distinct longer (Helmer et al., 2000; Viera et al., 2003). Only a handful of forest age classes can be reliably distinguished in single-date multispectral imagery. Age differences are blurred by differences in disturbance type and intensity that affect regrowth rates and related spectral responses during forest succession (Foody et al., 1996; Nelson et al., 2000; Thenkabail et al., 2004; Arroyo-Mora et al., 2005), although age explains more variability in rates of forest regrowth than does disturbance type (Helmer et al., 2010; Omeja et al., 2012).

Recently logged forest has less biomass than old-growth forest, but it may become spectrally indistinct from mature forest within a year or two (Asner et al., 2004a), which is another case in which the forest canopy recovers faster than forest AGLB. In a study in Sabah, Malaysia, conventional logging reduced forest biomass by 67%, but reduced impact logging reduced it by 44% (Pinard and Putz, 1996). In moist forests of Amazonia, AGLB decreased by only 11%–15% after reduced impact logging (Miller et al., 2011).

The youngest regenerating forest patches in landscapes usually do not dominate pixels as large as those of coarse-spatial-resolution

imagery like MODIS. The outcome is that maps from such imagery have high error rates for secondary tropical forest. When modeling pixel fractional cover of one or more young forest classes vs. nonforest vs. old forest with MODIS, for example, secondary forest is modeled with the most bias and the least precision (Braswell et al., 2003; Tottrup et al,. 2007). In Amazonia, the model R-square values for the fraction of secondary forest cover were 0.35 for MODIS data alone and 0.61 for MODIS plus MISR data. At the spatial resolution of 1.1 km, corresponding to most of the MISR bands, resulting maps overestimated secondary forest area by 26%. Converting fractional secondary forest cover to discrete classes underestimated secondary forest area by 43% (Braswell et al., 2003). Similarly, Carreiras et al. (2006) concluded that the errors for decision tree classification of secondary forest with SPOT 4 Vegetation across Amazonia were unacceptably high.

14.5.4 Detecting Tropical Forest Degradation with Multispectral Imagery

Tropical forests suffer anthropogenic pressures that perturb their structure and ecological functioning (Vitousek et al., 1994). Human activities that disturb them range from plant collection and human habitation to total deforestation. Many of these forest disturbances can occur at fine spatial scales of less than five to tens of meters, including forest fire (Aragão and Shimabukuro, 2010), recent logging (de Wasseige and Defourny, 2004; Asner et al., 2005; Sist and Ferreira, 2007), road networks (Laporte et al., 2007; Laurance et al., 2009), mining (Peterson and Heemskerk, 2001), and expanding agricultural frontiers (Dubreuil et al., 2012). These human impacts appear like small isolated objects within an ocean of greenness (Souza et al., 2003). They appear as points (logging gaps), lines (roads, trails), both points and lines (logging decks plus skid trails), and with mining areas, both bare soil and pooled water are present.

Although these disturbances can be small, medium-resolution remote sensing techniques can detect and quantify them within homogeneous forest cover (Gond et al., 2004). Compared with fine-scale imagery, images with pixels of 5–30 m have lower or no cost while more frequently covering larger areas of tropical forest. Consequently, medium-resolution imagery constitutes an excellent tool for assessing logging activities in tropical forests across large scales (Asner et al., 2005). Much work to detect finely scaled disturbances of tropical forests uses pixel-level spectra (Section 14.5.3.1). Other work models subpixel spectra to derive continuous variables for monitoring fine-scale disturbances, focusing on the degradation of forest C storage for REDD+ programs and ecosystem models (Section 14.5.3.2).

14.5.4.1 Detecting Fine-Scale Forest Degradation at the Pixel Level

Detecting small canopy gaps and skid trails that have been open for less than 6 months is possible in French Guiana with SPOT 5 HRG images (Gond and Guitet, 2009). The technique developed is based on the local contrast between a photosynthetically active surface (the forest) and one with no or little photosynthetic activity (the gap itself). Using the three main channels dedicated to vegetation identification (red [0.61–0.68 μm], near-infrared [0.79–0.89 μm] and SWIR [1.58–1.75 μm] wavelengths), the contrast between forests and gap is increased enough to be accurately depicted. The detection of an undisturbed forest pixel is made by multiple thresholds on the different reflectances. The advantage of standard remotely sensed data like SPOT 4/5 or Landsat 5/7/8 is the possibility to detect the focused object automatically (Pithon et al., 2013). The automatic processing makes the system operational for tropical forest management and depends only on image availability.

14.5.4.1.1 Road and Trail Detection

Road and trail detection is also a challenge for tropical forest management. Opening, active, and abandoned road and trail networks are a permanent landmark of tropical forest openness and degradation (Laurance et al., 2009). Documenting this dynamic is possible with the 30 years of medium-resolution radiometer archives (Landsat and SPOT). In 2007, Laporte et al. (2007) photo-interpreted Landsat imagery to map the road and trail network across the forests of Central Africa to show which forest areas are endangered by logging activity. When displaying red, NIR, and SWIR channels in red, green, and blue, active roads and trails are "brown"; abandoned roads and trails are "green," and intact tropical forests are "dark green" (de et al., 2004). To automatically process the archives for large areas, Bourbier et al. (2013) proposed a method for using Landsat archive to allow tropical forest managers to visualize the road and trail network dynamism at local (concession) or national scales.

14.5.4.1.2 Mining Detection

Detecting mining activity is slightly different. In general, detecting legal mining is not a real challenge because bare surfaces are prominent and easily mapped. When mining is illegal in tropical forests, however, the bare surface is much smaller and difficult to detect (Almeida-Filho and Shimabukuro, 2002). The additional difficulty comes from the mobility of the illegal miners. A recent abandoned mining site is detectable, but the miners have left. Detecting active mining sites where miners are illegally working is most critical to managers. To map active mining sites in French Guiana, an automatic system using SPOT 5 imagery from a local reception station has been operational since 2008 (Gond et al., unpublished). The system is based on detecting turbid waters resulting from debris washing. Again, the object "turbid water" sharply contrasts with its environment, as with tropical forest vs. bare soil. Using red, NIR, and SWIR channels, turbid water is detected by multiple thresholds on reflectances. So far, the operational system has processed over 1230 SPOT 5 images to ensure regular coverage in space and time of illegal mining activity in French Guiana (Joubert et al., 2012).

14.5.4.2 Detecting Forest Degradation at the Subpixel Level with Spectral Mixture Analysis

Forest degradation in the context of REDD+ can be defined as a persistent reduction in carbon stocks or canopy cover caused by sustained or high-impact disturbance. As a result, forest degradation is often expressed as a complex, three-dimensional change in forest structure related to the introduction of areas of bare soil, piles of dead vegetation created by the residues and collateral damage of removed trees and other plants, and areas with standing dead or damaged tree trunks associated with partial tree fall. Burned forests also leave surface fire scars, indicated by patches of charred vegetation and bare ground (Cochrane et al., 1999; Alencar et al., 2011). Much of tropical forest degradation occurring around the world is driven by selective logging and fires that escape into forests from neighboring clearings. At the multispectral sensor resolution of Landsat, SPOT, and MODIS, it is expected that forest degradation will be expressed in varying combinations of green vegetation (GV), soil, non-photosynthetic vegetation (NPV), and shade within image pixels.

Spectral mixture analysis (SMA) models can be used to decompose the mixture of GV, NPV, soil, and shade reflectances into component fractions known as endmembers (Adams et al., 1995). The SMA has been extensively used throughout the world's tropical forests to detect and map forest degradation (Asner et al., 2009a). For example, subpixel fractional cover of soils derived from the SMA was used to detect and map logging infrastructure including log landings and logging roads (Souza and Barreto, 2000), while the NPV fraction improved the detection of burned forests and of logging damage areas (Cochrane and Souza, 1998; Cochrane et al., 1999). GV and shade enhance the detection of canopy gaps created by tree fall (Asner et al., 2004b) and forest fires (Morton et al., 2011).

SMA models usually assume that the image spectra are formed by a linear combination of n pure spectra, or endmembers (Adams et al., 1995), such that

AQ11

$$R_b = \sum_{i=1}^{n} F_i R_{i,b} + \varepsilon_b \tag{14.4}$$

for

$$\sum_{i=1}^{n} F_i = 1 \tag{14.5}$$

where

R_b is the reflectance in band b
$R_{i,b}$ is the reflectance for endmember i, in band b
F_i is the fraction of endmember i
ε_b is the residual error for each band

The SMA model error is estimated for each image pixel by computing the RMS error, given by

$$\text{RMS} = \left[n^{-1} \sum_{b=1}^{n} \varepsilon_b \right]^{1/2} \tag{14.6}$$

As mentioned, in the case of degraded forests, the expected endmembers are GV, NPV, soil, and shade fractions. Including a cloud endmember is also possible, which improves the detection and masking of clouds when mapping forest degradation over large areas with long time series of imagery in the Amazon region (Souza et al., 2013). To calibrate the model, the endmembers can be obtained directly from the images (Small, 2004) or from reflectance spectra acquired in the field with a handheld spectrometer (Roberts et al., 2002). The advantage of obtaining endmembers directly from images is that spatial and radiometric calibration between field and sensor observations is not required. The SMA can be automated to make this technique useful for mapping and monitoring large tropical forest regions. A Monte Carlo unmixing technique using reference endmember bundles was proposed for that purpose (Bateson et al., 2000), as well as generic endmember spectral libraries (Souza et al., 2013).

14.5.4.3 Interpreting and Combining Subpixel Endmember Fractions and Derived Indices

The SMA fractions can be combined into indices to further accentuate areas of forest degradation. For example, the normalized difference fraction index (NDFI) was developed to enhance the detection of forest degradation by combining the detection capability of individual fractions (Souza et al., 2005). The NDFI values range from −1 to 1. For intact forests, NDFI values are expected to be high (i.e., about 1) due to the combination of high GV_{shade} (i.e., high GV and canopy shade) and low NPV and soil values. As forest becomes degraded, the NPV and soil fractions are expected to increase, lowering NDFI values relative to intact forest. Bare soil areas will produce NDFI value of −1 because of the absence of GV.

Another approach to SMA allows for uncertainty in the endmember reflectance spectra used for decomposing each pixel into constituent cover types. Referred to as endmember bundles (Bateson et al., 2000), SMA with spectral endmember variability provides a means to estimate GV, NPV, soil, and shade fractions with quantified uncertainty in each image pixel. Using a Monte Carlo approach, Asner and Heidebrecht (2002) developed automated SMA procedures that have subsequently been used to map forest degradation due to logging or understory fire in a wide variety of tropical regions (e.g., Alencar et al., 2011; Carlson et al., 2012; Allnutt et al., 2013; Bryan et al., 2013).

Several mapping algorithms based on spatial and contextual classifiers, decision trees, and change detection have also been applied to SMA results to better map forest degradation using Landsat, SPOT, and MODIS imagery. These techniques are

discussed elsewhere (Asner et al., 2009b; Souza and Siqueira, 2013). Additionally, large area mapping and estimates of forest degradation in the Amazon region have also been conducted using these techniques (Asner et al., 2005; Souza et al., 2013).

14.6 Mapping Tropical Forest Types with Multispectral Imagery

14.6.1 Forest Types as Strata for REDD+ and Other C Accounting

Maps of forest type are critical to tropical forest management, including for REDD+ and other GHG inventories. When estimating tropical forest AGLB and other C stores with existing inventory ground plots or lidar data, the estimates are generally stratified by forest type (Asner, 2009; Helmer et al., 2009; Salimon et al., 2011). When designing forest inventories or lidar surveys, stratifying sample locations by forest type improves the efficiency of the sample design (Wertz-Kanounnikoff, 2008), including stratification with types defined by disturbance history (Salk et al., 2013). Stratification by topography or geology may also be important (Ferry et al., 2010; Laumonier et al., 2010) if forest type does not inherently account for related variability in AGLB. An informative review and synthesis of lidar sample design as it relates to forest parameter estimation over large forest areas is available in Wulder et al. (2012). Another important role of forest-type maps based on multispectral satellite imagery is that they are often used to account for the distributions of species and habitats when planning representative reserve systems. For this reason, forest-type maps are also useful to identify where deforestation or wood harvesting is "leaking" to forests that are critical to conserve, but that store less C than forest areas being targeted in REDD+ or carbon offset projects.

Most satellite image–based maps of tropical forest types map classes of forest *formations*. Vegetation formations are defined by growth form and physiognomy. At the simplest level, forest formations may distinguish among closed, open, and wetland forests. More detailed formations may distinguish among forests with different leaf forms or phenology (e.g., deciduous vs. evergreen, broad-leaved vs. needle-leaved, or descriptors that imply a suite of physiognomic characteristics, such as "dry," "montane," or "cloud" forests). More detailed than forest formations are forest *associations*, which distinguish among tree species assemblages. For example, in Figure 14.5, which we discuss in Section 14.6.4, the upper-level headings for forests are forest formations. The subheadings under each forest formation are forest associations.

14.6.2 High-Resolution Multispectral Imagery for Mapping Finely Scaled Habitats

High-resolution imagery makes excellent reference data for calibrating classification and mapping models based on imagery with coarser spatial resolution, but using it as the primary basis for mapping forest types has several disadvantages. In high-resolution imagery, the within-stand spectral variability of forest types can be large, varying within tree crowns, for example, such that digital classifications at the pixel scale cannot distinguish many forest types. Also these images cover relatively small areas, making them inefficient for mapping forest types over large areas (Nagendra and Rocchini, 2008). Existing archives of high-resolution imagery also lack SWIR bands, which are important in vegetation mapping. Because Landsat ETM+ data have SWIR bands, for example, Thenkabail et al. (2003) found that three floristic tropical forest classes were more distinct in ETM+ data than in IKONOS imagery. Worldview 3, however, will have eight SWIR bands collected at a spatial resolution of 3.7 m.

Yet satellite imagery with high spatial resolution can aid in mapping finely scaled habitats or habitat characteristics. Example habitats are edges or linear features: riparian areas (Nagendra and Rocchini, 2008), roadsides or other corridors, or strands of vegetation types along coastlines. Habitats with high mechanical, chemical, or moisture stress can also be finely scaled. Example stresses are fast-draining substrates where microtopography strongly affects vegetation, like substrates of limestone (Martinuzzi et al., 2008) or sand, or substrates that are also semi-toxic like serpentines. High winds, or drier climate as in savanna ecotones, also lead to finely scale habitats.

Savanna ecosystems, for example, range in tree cover from grassland to forest, which is why we mention them here. Tree cover may change over meters, and high-resolution imagery may be most effective for habitat mapping. Boggs (2010) applied object-oriented classification to 4 m multispectral IKONOS imagery to map tree cover patterns in Mozambique savanna.

In Namibia, tree clusters and grass patches are distinguishable with object-oriented or pixel-level classifications of pan-sharpened QuickBird imagery (0.6 m pixels). In contrast, 10 m multispectral SPOT-5 pixels, though pan-sharpened to 2.5 m, required object-oriented classification (Gibbes et al., 2010).

Object-oriented classification of medium-resolution imagery can indeed sometimes substitute for high-resolution imagery when it can discern finer-scale features of interest that are missed with pixel-level classifications. In Jamaica, Newman et al. (2011) found that object-oriented classification of medium-resolution imagery led to better characterization of roads and forest fragmentation metrics than pixel-level classification did. Object-oriented classification of ASTER data can map savanna habitats in northwest Australia, and it was also more accurate than pixel-level classification (Whiteside et al., 2011). Longer-wave infrared bands were resampled to the 15 m resolution of the visible and NIR bands.

14.6.3 Remote Tree Species Identification and Forest-Type Mapping

Many tropical tree species can be identified by photo interpretation of high-resolution satellite imagery or air photos. With tree crowns in tropical forest often reaching >10 m in diameter,

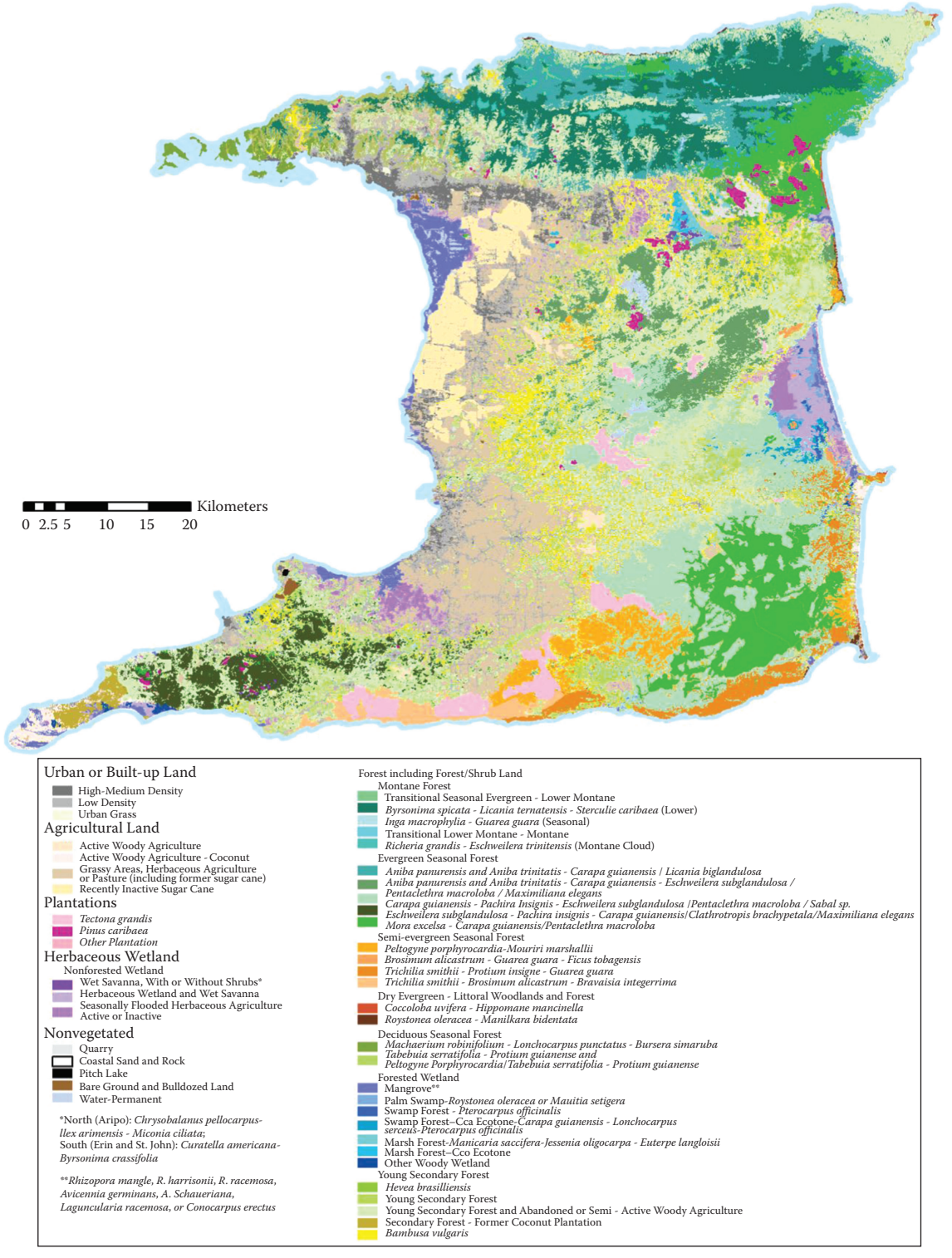

FIGURE 14.5 Forest associations and land cover were mapped with the gap-filled Landsat ETM+ imagery, centered around the year 2007, plus synthetic multiseason imagery developed from three gap-filled TM images from the 1980s that were from the mid to late dry season including from severe drought.

subcrown features are visible. In subtropical to warm-temperate forests of east central Queensland, Australia, Tickle et al. (2006) correctly identified dominant tree species in most of 150 air photo plots with stereo color air photos of scale 1:4000 (~2 m resolution). With these data, they categorized the air photo plots into five genus groups.

In moist forests of Panama, Garzón-López et al. (2013) found that visual analysis of high-resolution color air photos (0.13 m pixels) can reveal spatial distributions of some tropical forest canopy trees. Of 50 common canopy species on a 50 ha plot, 22% had crowns that were distinct in the photos. Of four species tested, interpreters found 40% of the stems that were recorded in field surveys; the resulting maps accurately showed spatial patterns of the species. Sánchez-Azofeifa et al. (2011) concluded that 2.4 m multispectral QuickBird imagery can reveal the spatial distribution and clusters of a species that is conspicuous when flowering, though immature or nonflowering individuals are often missed.

In French Guiana, Trichon and Julien (2006) found that 12 of the 15 most common canopy species or species groups were identifiable, with an accuracy of 87%, in color air photos ranging in scale from 1:1500 to 1:8000 (~0.75 to 4 m pixels). In the photos, 20%–25% of trees with dbh $\geq$ 10 cm, and all trees with dbh $\geq$ 20 cm, were visible. For 10 taxa from old-growth Ecuadorian Amazon forest representing a range of crown structures, González-Orozco et al. (2010) found that photo interpretation of large-scale air photos with a dichotomous key correctly identified individuals at a rate of >70% for three of the taxa and >50% for two of them.

That photo interpreters can identify many of the dominant species in tropical forest canopies in high-resolution imagery suggests that, given field-based knowledge of the composition and distribution of tree floristic classes (i.e., tree species associations), which are defined by dominant tree species, floristic types of tropical forest can be identified in high-resolution multispectral imagery. Consequently, reference data from photo-interpreting high-resolution multispectral imagery can supplement field data as a source of training and validation data for mapping tropical tree communities with satellite imagery (Helmer et al., 2012).

14.6.4 Mapping Tropical Forest Types with Medium-Resolution Imagery

In mapping tropical forest types with multispectral imagery, spectral similarity among forest classes is a major challenge. Disturbance, differences in topographic illumination, artifacts from filling cloud and other data gaps or from scene mosaicing, all increase class signature variability and consequently increase signature overlap among classes. Secondary forest in a humid montane zone, for example, may be spectrally similar to shade coffee or old-growth forest on highly illuminated slopes. When on a shaded slope, that same secondary montane forest is spectrally similar to old-growth forest in a less productive zone at higher altitudes (Helmer et al., 2000). Yet digital classifications of multispectral imagery can map many different forest types with some additions: (1) ancillary geographic data, (2) multiseason or multiyear imagery or derived phenology, and (3) pixels for training classification models that represent the variability in environmental and image conditions.

Digital maps of environmental data like topography, climate, or geology help distinguish spectrally similar forest types. With Landsat TM/ETM+, linear discriminant function classifications have incorporated ancillary data via post-classification rules based on topography to map eucalyptus forest types (Skidmore, 1989); adding topographic bands to spectral bands to map land-cover and forest physiognomic types (Elomnuh and Shrestha 2000; Helmer et al., 2002; Gottlicher et al., 2009) or distinguish among tree floristic classes (Foody and Cutler, 2003; Salovaara et al., 2005); and classifying imagery by geoclimatic zone (Helmer et al., 2002). Image smoothing or segmentation can improve these classifications by reducing within-class spectral variation (Tottrup, 2004; Thessler et al., 2008).

Tree associations or other floristic classes can be separable with multispectral imagery within an ecological zone, particularly if topographic bands are included. With TM/ETM+ and 18–127 plots, studies have separated three to nine floristic classes within lowland evergreen forest in central Africa, Amazonia, Borneo, or Costa Rica (Foody and Cutler, 2003; Thenkabail et al., 2003; Salovaara et al., 2005; Thessler et al., 2008; Sesnie et al., 2010). Chust et al. (2006) mapped nine floristic subclasses with ETM+ data, elevation, and geographic position over a broad environment across central Panama. With Landsat TM data, Wittmann et al. (2002) mapped three structural classes of Amazonian várzea forests that corresponded to four associations: early successional low várzea, late secondary and climax low várzea (two associations), and climax high várzea. These studies use spectral data from a single image date and consider only forest; cloudy areas were mapped as such.

When mapping many classes, machine learning classifications more effectively incorporate ancillary environmental data including date bands for gap-filled images. They also do not assume that class spectral distributions are parametric, and they typically outperform linear classifications. Combining ancillary data and machine learning classification permits classifications that distinguish many forest and land-cover types, even with noisy, cloud-gap-filled imagery. Examples with TM/ETM+ include decision tree classifications of one or two seasons of cloud-gap-filled Landsat plus ancillary data to map tropical forest physiognomic types and land cover (Kennaway and Helmer, 2007; Helmer et al., 2008; Kennaway et al., 2008). Sesnie et al. (2008) mapped land cover, agriculture type, floristic classes of lowland old-growth forest and three higher-elevation classes based on a map of life zones (*sensu* Holdridge, 1967) with a relatively cloud-free image for each of two scenes. To map tree floristic classes of lowland through montane tropical forest types and land cover in Trinidad and Tobago, Helmer et al. (2012) applied decision tree classification to recent cloud-gap-filled Landsat imagery stacked with decades-old, gap-filled synthetic multiseason imagery from droughts (Figure 14.5).

Mapping many physiognomic or floristic classes of tropical forest as in the earlier studies requires (1) thousands of training and testing pixels representing the environmental and spectral ranges of each class, including the range of pixel dates where gap-filled imagery was used (Helmer and Ruefenacht, 2007); (2) a band that represents the date of the source image for each pixel in the composite image (a *date band*); and a machine learning classification model. The extensive training data needed are rarely available from field plots. But analysts can learn to identify many physiognomic and floristic classes in remotely sensed imagery given field-based knowledge of general distributions, particularly given free viewing of high-resolution imagery online and Landsat image archives, allowing almost unlimited reference data collection.

Helmer et al. (2012) found that all mono- and bidominant tree floristic classes and many other tree communities in Trinidad and Tobago could be distinguished in reference imagery from nearby associations by (1) unique canopy structure in high-resolution imagery or (2) distinct or unique phenology on specific dates of either high- or medium-resolution reference imagery. For example, distinct canopy structure at high resolution distinguished *Mora excelsa* forests, littoral associations (frequent palms in one; prostrate stems in the other); *Pterocarpus officinalis* swamps, palm swamps, mangroves, and stands of bamboo (*Bambusa vulgaris*), abandoned coconut (*Cocos nucifera*), teak (*Tectona grandis*), pine (*Pinus caribaea*), and Brazilian rubber (*Hevea brasiliensis*). Phenology, including characteristics like flowering, deciduousness, leaf flushes, or inundation, helped to distinguish seven forest associations in high-resolution reference imagery and four associations in phenologically unique Landsat reference scenes. With this knowledge and reference imagery, thousands of training data pixels could be collected.

Including multiseason imagery in classification models of coarse-resolution imagery also improves spectral distinction among tropical forest types (Bohlman et al., 1998, Tottrup, 2004). What is exciting is that we can now think beyond multiseason imagery to multiyear imagery that captures climate or weather extremes or disturbance history. Helmer et al. (2012) found that adding bands from cloud-gap-filled TM imagery from a severe drought that occurred 20 years earlier than the most recent imagery used in the stack of data for classification contributed to the largest increases in accuracy when mapping forest associations in Trinidad. Mapping accuracy of seasonal associations benefited the most. Accuracy improved by 14%–21% for deciduous, 7%–36% for semievergreen, and 3%–11% for seasonal evergreen associations, and by 5%–8% for secondary forest and woody agriculture. Multiyear multispectral imagery that displays different flood stages helps distinguish between upland and periodically flooded tropical forests (Helmer et al., 2009) and among tropical forested wetland types (and can reflect differences in secondary forest species composition by mapping disturbance type as mentioned) (Helmer et al., 2010). In Amazonia, de Carvalho et al. (2013) determined the life cycle length of native bamboo patches with multiyear TM/ETM+ data.

14.6.5 Species Richness and Multispectral Imagery

The tree species richness of tropical forests increases with some of the same variables that influence forest reflectance in multispectral satellite imagery. Richness increases with forest height (among lowland forests with strong edaphic differences), soil fertility (after accounting for rainfall), canopy turnover, and time since catastrophic disturbance; richness decreases with dry season length, latitude, and altitude (Givnish, 1999). We know from forest ground plots that tree species richness also increases with secondary forest age (Whittmann et al., 2002; Chazdon et al., 2007; Helmer et al., 2008). Consequently, over gradients that span from dry to humid, multispectral bands and indices related to vegetation greenness, structure, or disturbance may correlate with species richness. And in fact studies have documented such relationships with single-date Landsat TM or ETM+ imagery (Foody and Cutler, 2006; Nagendra et al., 2010; Hernández-Stefanoni et al., 2011). Single-date multispectral data are unlikely, however, to be sensitive to differences in species richness along short environmental gradients such as among humid evergreen tropical forests. Moreover, an important consideration in biodiversity conservation is that species richness alone does not define conservation value: representation across as many native ecosystems and species as possible is just as important if not more so. Many less productive tropical forest types with less tree species richness, like cloud forests, or forests on harsh or drying soils like those on ultramafic or limestone substrates or ombrotrophic sands, have the most endemic species richness. AQ12

14.6.6 Tropical Forest-Type Mapping at Coarse Spatial Scale

In tropical regions extending over large areas, multiseason data from monthly, annual, or multiyear composites of imagery with coarse spatial resolution have supported large-area mapping of tropical forest formations with even linear classification methods (Joshi et al., 2006; Gond et al., 2011, 2013; Pennec et al., 2011; Verheggen et al., 2012). For example, Gond et al. (2011) mapped five classes of forest canopy openness across the French Guiana with an unsupervised classification of an annual composite image of SPOT 4 Vegetation data. Across Central Africa, Gond et al. (2013) mapped 14 forest formations with 1 year of 8- and 16-day MODIS image composites. The forest formations were based on leaf phenology and canopy openness. With 1 year of NDVI composite images from the Indian Resource Satellite (IRS 1C) WiFS across India, Joshi et al. (2011) mapped 14 forest formations. The formations were labeled by phenology and climatic class (e.g., *Tropical dry deciduous forest*, *Tropical moist deciduous forest*, and so on). Verheggen et al. (2012) applied unsupervised classification to seasonal and annual composites of MEdium-Resolution Imaging Spectrometer (MERIS) and SPOT 4 Vegetation data for the Congo basin, producing a map with six forest classes that were based on leaf phenology, canopy

openness, and elevation class. Producers' and users' accuracies for forest classes in the latter two studies were mostly between 80% and 100%.

Combining ancillary data, monthly image composites of imagery with coarse spatial resolution but high temporal resolution, and decision tree classification has permitted forest classifications at subcontinental to global scales or has distinguished many more forest formations. Decision tree classification of monthly composites of imagery with coarse spatial resolution, and mosaics of such composites, is also used to map tropical forests over large areas. Examples of such large-area maps based on MODIS image composites are of tropical forest ecoregion (Muchoney et al., 2000), biome (Friedl et al., 2002), or forest formation (Carreiras et al., 2006). With decision tree classification of dry season MODIS image composites, Portillo-Quintero and Sánchez-Azofeifa (2010) mapped the extent of two classes of tropical dry forests (T*ropical dry forest* and *Forests in tropical grasslands, savannas, and shrublands*), for the mainland Neotropics plus the Greater Antilles. Overall accuracy was 82%. The importance of this latter work is that global land-cover maps often misclassify dry tropical forests as some other land cover.

14.6.7 Tropical Forest-Type Mapping and Image Spatial Resolution

Without question, multiseason data greatly improve the number of different physiognomic or floristic classes of tropical forest that can be mapped with multispectral satellite imagery. Monthly image composites or derived phenology metrics, as are possible with coarse-resolution imagery, are optimal. Joshi et al. (2006) qualitatively compared their WiFS-based map of forest types across India with a forest map of the country based on LISS data, which has a pixel resolution of 23.5 m but a 24-day repeat cycle. They concluded that the 5-day revisit cycle of WiFS, which allowed them to incorporate 12 monthly image composites, yielded better information on forest types and other vegetation and land-cover classes, even though WiFS has a spatial resolution of 188 m.

However, tropical forest types can change greatly over small areas, and spatial resolutions coarser than 100–200 m are too coarse to distinguish important differences in forest types in many places. In tropical islands, for example, forest floristic and physiognomic types that are critical to distinguish for conservation planning would be poorly delineated. Medium-resolution imagery with a shorter revisit cycle would greatly improve prospects for mapping tropical forest types with multispectral imagery. This could be more easily accomplished, for example, if AWiFS data, with its 56 m spatial resolution and 5-day revisit cycle, were available for all of the tropics, or if the Landsat program had a constellation of at least four satellites.

In addition, past disturbances affect forest physiognomy and species composition, and some forest classes may become spectrally distinct only during periodic drought and flooding. Consequently, forest-type mapping can also benefit when older satellite imagery or long image time series are incorporated into forest-type mapping, as in Helmer et al. (2010, 2012).

Finally, to distinguish tropical forest types on small mountains, small islands, along coastlines, rivers, and other linear features, or in other finely scaled landscapes, high-resolution imagery will be needed.

14.7 Monitoring Effects of Global Change on Tropical Forests

14.7.1 Progress in Monitoring Tropical Forests at Subcontinental to Global Scales

Tropical forest mapping with coarse-resolution imagery in optical remote sensing is very constrained by cloud cover. Helpfully, its high temporal frequency of acquisition balances the handicaps of cloud-contaminated pixels (McCallum et al., 2006). Historical long time series from NOAA-AVHRR paved the way for this research (Tucker et al., 1985; Townshend et al., 1991). Indeed, the spectral capacities from visible to SWIR of these sensors motivated many applications and technological developments. The identification of tropical forest patterns has improved over time (Holben, 1986; Mayaux et al., 1998; DeFries et al., 2000) and benefits from a large panel of vegetation indices for evaluating photosynthetic activity (Rouse et al., 1974; Huete, 1988; Pinty and Verstraete, 1992; Qi et al., 1994; Gao, 1996).

At the end of the 1990s, the experiences gained from these applications led to new sensors adapted to land surface observation, including SPOT Vegetation (March 1998) and TERRA-MODIS (December 1999) (Friedl et al., 2010). Spatial resolutions were improved from 1.1 km (NOAA-AVHRR) to 1.0 km (Vegetation), 0.3 (MERIS), and 0.5/0.25 km (MODIS). Geo-location was improved. Specific spectral bands dedicated to vegetation were implemented. New sensor technology was developed such as the push-broom system on Vegetation, which avoids large swath distortions. After 15 years of feedback, we may now measure the added value of these sensors.

Research to characterize tropical forests at subcontinental to global scales has become more accurate and precise (Mayaux et al., 2004; Vancutsem et al., 2009) by taking phenology into account (Xiao et al., 2006; Myneni et al., 2007; Doughty and Goulden, 2008; Park, 2009; Brando et al., 2010). Repetitive observation and long temporal archives make possible land-surface observation on 8-, 10-, or 16-day time periods and allow phenology studies to take advantage of both high spectral quality and high observation frequency (Verheggen et al., 2012 for MERIS and Vegetation; Gond et al., 2013 for MODIS). In addition, there are more forest attributes being characterized, including forest edges (to delimit forest patches and more accurately estimate forest areas) (Verheggen et al., 2012; Mayaux et al., 2013), aboveground biomass (Malhi et al., 2006; Saatchi et al., 2007; Baccini et al., 2008), deforestation and forest degradation (Achard et al., 2002; Duveiller et al., 2008; Hansen et al., 2008; Baccini et al., 2012; Desclée et al., 2013), and climate change impacts (Phillips et al., 2009; Lewis et al., 2011; Samanta et al., 2011).

Sensor capabilities and computer capacities now allow the production of global-scale land-cover maps (Bartholomé and Belward, 2005, for Vegetation; Friedl et al., 2002; Hansen et al., 2008, for MODIS), which have greatly improved our knowledge of land surface cover in comparison with previous views obtained from NOAA-AVHRR (DeFries and Townshend, 1994; Loveland and Belward, 1997).

Tropical forest characterizations with multispectral imagery have now begun to address a real challenge: that of monitoring and understanding climate change impacts on the biosphere (Gibson et al., 2011). Tropical forests are particularly threatened by global temperature increases and the possibility of modified rainfall regimes (Zelazowski et al., 2011). These changes will influence vegetation spatial distribution (Parmesan and Yohe, 2003), forest functioning (Nemani et al., 2003), and carbon storage capacity (Stephens et al., 2007), which may in turn affect climate. In this context, monitoring tropical forests with coarse-resolution satellite imagery is of prime importance to understanding biological processes and managing forest resilience. Zhao and Running (2010), for example, showed that large-scale droughts have decreased net primary productivity in the Southern Hemisphere, including tropical Asia and South America. As we discuss later, however, some critical remote sensing problems still need to be addressed before we can effectively monitor some important effects of droughts on tropical forests.

14.7.2 Feedbacks between Tropical Forest Disturbance and Drought

Multispectral imagery can help characterize the positive feedback among tropical forest disturbance, fire, and climate. First, tropical forest clearing dries nearby forest, and multispectral imagery can detect forest clearing. In Amazonia, for example, Briant et al. (2010) delineated forest boundaries with MODIS multispectral bands and found that as the forest becomes more fragmented, drops in MODIS-based indices related to canopy moisture extend further into intact forest, and that the old forest in more fragmented landscapes has lower canopy moisture to begin with. Second, forest cover data also reveal that forests desiccated by fragmentation and other disturbance are more susceptible to fire. Armenteras et al. (2013) used forest fragmentation indices from forest cover maps, along with active fire data from MODIS, which uses MODIS thermal bands, to show that forest fires increase in extent and frequency with fragmentation. Logging also increases forest vulnerability to fire (Uhl and Buschbacher, 1985; Woods, 1989), and as outlined earlier, logging can be detected with medium-resolution multispectral imagery.

A third aspect of the disturbance–fire–climate feedback is that drought magnifies the association between disturbance and fire (Siegert et al., 2001; Alencar et al., 2006). In Amazonia, fire scars mapped with Landsat occurred mostly within 1 km of clearings during normal dry seasons but extended to 4 km from clearings during drought years (Alencar et al., 2006). Some of these studies relied on Landsat imagery to quantify forest fragmentation, because of its finer spatial resolution, or radar imagery to map fire scars, to avoid clouds.

Amazonian droughts are likely to become more common and severe with climate change. During droughts, reduced forest growth and increased tree mortality cause intact forests to shift from a net sink to a net source of CO_2 to the atmosphere (Lewis et al., 2011). However, monitoring drought effects that are spectrally subtle, like increased tree mortality or changes in phenology, remains a challenge because of residual cloud and aerosol contamination in coarse-resolution multispectral imagery. For example, studies have found that vegetation greenness may increase, decrease, or show no change during drought. The increases could stem from decreased cloud cover, leaf flushes related to increased sunlight, decreased canopy shadow from increased mortality of the tallest trees, or all three of these factors, and despite observation frequency, cloud and smoke contamination in pixels still obscures trends in vegetation greenness (Anderson et al., 2010; Asner and Alencar, 2010; Samanta et al., 2010). Asner et al. (2004c) suggest that metrics from hyperspectral imagery may be better suited to resolve drought effects on tropical forests because they are sensitive to canopy leaf water content and light-use efficiency. A challenge, then, is to develop a system that, despite cloud and smoke contamination, integrates these different sensors to continuously monitor the feedback between forest fragmentation, logging, fire, and climate.

14.8 Summary and Conclusions

Across spatial scales, increased image access, and data usability are the main factors driving an explosion of progress in characterizing tropical forests with multispectral satellite imagery. The menu of preprocessed image products of the second generation of high-frequency earth observation satellite sensors, MODIS and SPOT Vegetation, along with their improved spatial and spectral resolution, led to a wider group of users applying multispectral imagery across larger areas and in more diverse ways. Products like cloud-screened composites of earth surface reflectance, vegetation indices, quality flags, fire flags, and land cover have enabled efforts to map tropical forest productivity, type, phenology, moisture status, and biomass, and to study the effects of climate change on tropical forests, particularly feedback among drought, fire, and deforestation.

At the scale of medium-resolution imagery, free access to Landsat, and in some cases free access to SPOT imagery, has spawned many new applications that rely on dozens, hundreds, or thousands of scenes, including scenes with scan-line gaps or scenes previously considered too cloudy to bother with. Cloud- and gap-filled Landsat imagery and image time series are now used to automatically detect forest clearing, partial disturbance, or regrowth; quantify degradation of tropical forest C storage; map the age, structure, biomass, height, and disturbance type of secondary tropical forests; automatically and more precisely mask clouds and cloud shadows in imagery; and create detailed maps of forest types in these often cloudy landscapes.

Characterizing tropical forest phenology at medium resolution will now be possible for many places, which will be easier given recent additions to Landsat image preprocessing. Many of these automated applications build on the experiences gained from the high-frequency, coarse-spatial-resolution imagery, and all of them are relevant to REDD+ monitoring, reporting, and verification.

At fine spatial scales, free viewing and low-cost printing of georeferenced high-resolution imagery via online tools like Google Earth and Bing supplement field data for training and testing the earlier products that are based on medium- and coarse-resolution imagery. In addition, scientists have used image products from Google Earth to estimate tropical forest biomass directly. New commercial sensors that produce multispectral satellite imagery with spatial resolutions ≤0.5 m should also allow more disturbance types and tropical tree communities to be remotely identifiable.

Acknowledgments

Thanks to John Armston and Ariel Lugo for their invaluable comments on this text. This research was conducted in cooperation with the University of Puerto Rico and the USDA Forest Service Rocky Mountain Research Station.

References

Achard, F., Eva, H. D., Stibig, H.-J., Mayaux, P., Gallego, J., Richards, T., and Malingreau, J.-P. 2002. Determination of deforestation rates of the world's humid tropical forests. *Science*, 297, 999–1002.

Ackerman, S., Holz, R., Frey, R., Eloranta, E., Maddux, B., and McGill, M. 2008. Cloud detection with MODIS. Part II: Validation. *Journal of Atmospheric and Oceanic Technology*, 25, 1073–1086.

Adams, J. B., Sabol, D. E., Kapos, V., Almeida Filho, R., Roberts, D. A., Smith, M. O., and Gillespie, A. R. 1995. Classification of multispectral images based on fractions of endmembers: Application to land-cover change in the Brazilian Amazon. *Remote Sensing of Environment*, 52, 137–154.

Ahmed, O. S., Franklin, S. E., and Wulder, M. A. 2014. Interpretation of forest disturbance using a time series of Landsat imagery and canopy structure from airborne lidar. *Canadian Journal of Remote Sensing*, 39, 521–542.

Alencar, A., Nepstad, D., and Diaz, M. C. V. 2006. Forest understory fire in the Brazilian Amazon in ENSO and non-ENSO years: Area burned and committed carbon emissions. *Earth Interactions*, 10, 1–17.

Alencar, A., Asner, G. P., Knapp, D., and Zarin, D. 2011. Temporal variability of forest fires in eastern Amazonia. *Ecological Applications*, 21, 2397–2412.

Allnutt, T. F., Asner, G. P., Golden, C. D., and Powell, G. V. 2013. Mapping recent deforestation and forest disturbance in northeastern Madagascar. *Tropical Conservation Science*, 6, 1–15.

Almeida-Filho, R. and Shimabukuro, Y. E. 2002. Digital processing of a Landsat-TM time series for mapping and monitoring degraded areas caused by independent gold miners, Roraima State, Brazilian Amazon. *Remote Sensing of Environment*, 79, 42–50.

Anderson, L. O., Malhi, Y., Aragão, L. E., Ladle, R., Arai, E., Barbier, N., and Phillips, O. 2010. Remote sensing detection of droughts in Amazonian forest canopies. *New Phytologist*, 187, 733–750.

Aragão, L. E. and Shimabukuro, Y. E. 2010. The incidence of fire in Amazonian forests with implications for REDD. *Science*, 328, 1275–1278.

Armenteras, D., González, T. M., and Retana, J. 2013. Forest fragmentation and edge influence on fire occurrence and intensity under different management types in Amazon forests. *Biological Conservation*, 159, 73–79.

Arroyo-Mora, J. P., Sánchez-Azofeifa, G. A., Kalacska, M. E., Rivard, B., Calvo-Alvarado, J. C., and Janzen, D. H. 2005. Secondary forest detection in a Neotropical dry forest landscape using Landsat 7 ETM+ and IKONOS Imagery1. *Biotropica*, 37, 497–507.

Asner, G. P. and Heidebrecht, K. B. 2002. Spectral unmixing of vegetation, soil and dry carbon cover in arid regions: Comparing multispectral and hyperspectral observations. *International Journal of Remote Sensing*, 23, 3939–3958.

Asner, G. P., Palace, M., Keller, M., Pereira, R., Silva, J. N., and Zweede, J. C. 2002. Estimating canopy structure in an Amazon forest from laser range finder and IKONOS satellite observations 1. *Biotropica*, 34, 483–492.

Asner, G. P., Keller, M., Pereira, R., Zweede, J. C., and Silva, J. N. 2004a. Canopy damage and recovery after selective logging in Amazonia: Field and satellite studies. *Ecological Applications*, 14, 280–298. AQ13

Asner, G. P., Keller, M., and Silva, J. N. 2004c. Spatial and temporal dynamics of forest canopy gaps following selective logging in the eastern Amazon. *Global Change Biology*, 10, 765–783. AQ14

Asner, G. P., Nepstad, D., Cardinot, G., and Ray, D. 2004b. Drought stress and carbon uptake in an Amazon forest measured with spaceborne imaging spectroscopy. *Proceedings of the National Academy of Sciences of the United States of America*, 101, 6039–6044.

Asner, G. P., Knapp, D. E., Broadbent, E. N., Oliveira, P. J., Keller, M., and Silva, J. N. 2005. Selective logging in the Brazilian Amazon. *Science*, 310, 480–482.

Asner, G. P. 2009. Tropical forest carbon assessment: Integrating satellite and airborne mapping approaches. *Environmental Research Letters*, 4, 034009.

Asner, G. P., Knapp, D. E., Balaji, A., and Páez-Acosta, G. 2009a. Automated mapping of tropical deforestation and forest degradation: CLASlite. *Journal of Applied Remote Sensing*, 3, 033543–033543–033524. AQ15

Asner, G. P., Rudel, T. K., Aide, T. M., Defries, R., and Emerson, R. 2009b. A contemporary assessment of change in humid tropical forests. *Conservation Biology*, 23, 1386–1395.

Asner, G. P. and Alencar, A. 2010. Drought impacts on the Amazon forest: The remote sensing perspective. *New Phytologist*, 187, 569–578.

Asner, G. P., Mascaro, J., Muller-Landau, H. C., Vieilledent, G., Vaudry, R., Rasamoelina, M., Hall, J. S. et al. 2012. A universal airborne LiDAR approach for tropical forest carbon mapping. *Oecologia*, 168, 1147–1160.

Asner, G. P., Mascaro, J., Anderson, C., Knapp, D. E., Martin, R. E., Kennedy-Bowdoin, T., van Breugel, M. et al. 2013. High-fidelity national carbon mapping for resource management and REDD+. *Carbon Balance and Management*, 8, 1–14.

Avitabile, V., Baccini, A., Friedl, M. A., and Schmullius, C. 2012. Capabilities and limitations of Landsat and land cover data for aboveground woody biomass estimation of Uganda. *Remote Sensing of Environment*, 117, 366–380.

Baccini, A., Laporte, N., Goetz, S., Sun, M., and Dong, H. 2008. A first map of tropical Africa's above-ground biomass derived from satellite imagery. *Environmental Research Letters*, 3, 045011.

Baccini, A., Goetz, S., Walker, W., Laporte, N., Sun, M., Sulla-Menashe, D., Hackler, J. et al. 2012. Estimated carbon dioxide emissions from tropical deforestation improved by carbon-density maps. *Nature Climate Change*, 2, 182–185.

Barbier, N., Couteron, P., Proisy, C., Malhi, Y., and Gastellu-Etchegorry, J. P. 2010. The variation of apparent crown size and canopy heterogeneity across lowland Amazonian forests. *Global Ecology and Biogeography*, 19, 72–84.

Bartholomé, E. and Belward, A. 2005. GLC2000: A new approach to global land cover mapping from Earth observation data. *International Journal of Remote Sensing*, 26, 1959–1977.

Bateson, C. A., Asner, G. P., and Wessman, C. A. 2000. Endmember bundles: A new approach to incorporating endmember variability into spectral mixture analysis. *IEEE Transactions on Geoscience and Remote Sensing*, 38, 1083–1094.

Blackard, J., Finco, M., Helmer, E., Holden, G., Hoppus, M., Jacobs, D., Lister, A. et al. 2008. Mapping US forest biomass using nationwide forest inventory data and moderate resolution information. *Remote Sensing of Environment*, 112, 1658–1677.

Boggs, G. 2010. Assessment of SPOT 5 and QuickBird remotely sensed imagery for mapping tree cover in savannas. *International Journal of Applied Earth Observation and Geoinformation*, 12, 217–224.

Bohlman, S. A., Adams, J. B., Smith, M. O., and Peterson, D. L. 1998. Seasonal foliage changes in the eastern Amazon basin detected from Landsat Thematic Mapper satellite images. *Biotropica*, 30, 13–19.

AQ16 Bontemps, S., Arino, O., Bicheron, P., Carsten Brockmann, C., Leroy, M., Vancutsem, C., and Defourny, P. 2012. Operational service demonstration for global land-cover mapping. The GlobCover and GlobCorine experiences for 2005 and 2009, in *Remote Sensing of Land Use and Land Cover: Principles and Applications*, C. Giri (ed.). Terre Haute, IN: CRC Press, pp. 243–264.

Bourbier, L., Cornu, G., Pennec, A., Brognoli, C., and Gond, V. 2013. Large-scale estimation of forest canopy opening using remote sensing in Central Africa. *Bios et Forets des Tropiques*, 67, 3–9. AQ17

Boyd, D. S., Foody, G. M., Curran, P., Lucas, R., and Honzak, M. 1996. An assessment of radiance in Landsat TM middle and thermal infrared wavebands for the detection of tropical forest regeneration. *International Journal of Remote Sensing*, 17, 249–261.

Brando, P. M., Goetz, S. J., Baccini, A., Nepstad, D. C., Beck, P. S., and Christman, M. C. 2010. Seasonal and interannual variability of climate and vegetation indices across the Amazon. *Proceedings of the National Academy of Sciences*, 107, 14685–14690.

Braswell, B., Hagen, S., Frolking, S., and Salas, W. 2003. A multivariable approach for mapping sub-pixel land cover distributions using MISR and MODIS: Application in the Brazilian Amazon region. *Remote Sensing of Environment*, 87, 243–256.

Briant, G., Gond, V., and Laurance, S. G. 2010. Habitat fragmentation and the desiccation of forest canopies: A case study from eastern Amazonia. *Biological Conservation*, 143, 2763–2769.

Bryan, J. E., Shearman, P. L., Asner, G. P., Knapp, D. E., Aoro, G., and Lokes, B. 2013. Extreme differences in forest degradation in Borneo: Comparing practices in Sarawak, Sabah, and Brunei. *PloS One*, 8. AQ18

Carlson, K. M., Curran, L. M., Ratnasari, D., Pittman, A. M., Soares-Filho, B. S., Asner, G. P., Trigg, S. N. et al. 2012. Committed carbon emissions, deforestation, and community land conversion from oil palm plantation expansion in West Kalimantan, Indonesia. *Proceedings of the National Academy of Sciences*, 109, 7559–7564.

Carreiras, J., Pereira, J., Campagnolo, M. L., and Shimabukuro, Y. E. 2006. Assessing the extent of agriculture/pasture and secondary succession forest in the Brazilian Legal Amazon using SPOT VEGETATION data. *Remote Sensing of Environment*, 101, 283–298.

Castillo-Santiago, M. A., Ricker, M., and de Jong, B. H. 2010. Estimation of tropical forest structure from SPOT-5 satellite images. *International Journal of Remote Sensing*, 31, 2767–2782.

Chazdon, R. L., Letcher, S. G., Van Breugel, M., Martínez-Ramos, M., Bongers, F., and Finegan, B. 2007. Rates of change in tree communities of secondary Neotropical forests following major disturbances. *Philosophical Transactions of the Royal Society B: Biological Sciences*, 362, 273–289.

Choi, H. and Bindschadler, R. 2004. Cloud detection in Landsat imagery of ice sheets using shadow matching technique and automatic normalized difference snow index threshold value decision. *Remote Sensing of Environment*, 91, 237–242.

Chust, G., Chave, J., Condit, R., Aguilar, S., Lao, S., and Pérez, R. 2006. Determinants and spatial modeling of tree β-diversity in a tropical forest landscape in Panama. *Journal of Vegetation Science*, 17, 83–92.

Cochrane, M. and Souza Jr, C. 1998. Linear mixture model classification of burned forests in the eastern Amazon. *International Journal of Remote Sensing*, 19, 3433–3440.

Cochrane, M. A., Alencar, A., Schulze, M. D., Souza, C. M., Nepstad, D. C., Lefebvre, P., and Davidson, E. A. 1999. Positive feedbacks in the fire dynamic of closed canopy tropical forests. *Science*, 284, 1832–1835.

Couteron, P., Pelissier, R., Nicolini, E. A., and Paget, D. 2005. Predicting tropical forest stand structure parameters from Fourier transform of very high-resolution remotely sensed canopy images. *Journal of Applied Ecology*, 42, 1121–1128.

Crist, E. P. and Cicone, R. C. 1984. A physically-based transformation of Thematic Mapper data—The TM Tasseled Cap. *IEEE Transactions on Geoscience and Remote Sensing*, 22, 256–263.

de Carvalho, A. L., Nelson, B. W., Bianchini, M. C., Plagnol, D., Kuplich, T. M., and Daly, D. C. 2013. Bamboo-dominated forests of the southwest Amazon: Detection, spatial extent, life cycle length and flowering waves. *PloS One*, 8, e54852.

de Wasseige, C. and Defourny, P. 2004. Remote sensing of selective logging impact for tropical forest management. *Forest Ecology and Management*, 188, 161–173.

DeFries, R. and Townshend, J. 1994. NDVI-derived land cover classifications at a global scale. *International Journal of Remote Sensing*, 15, 3567–3586.

DeFries, R., Hansen, M., Townshend, J., Janetos, A., and Loveland, T. 2000. A new global 1-km dataset of percentage tree cover derived from remote sensing. *Global Change Biology*, 6, 247–254.

Degagne, R. S., Henkel, T. W., Steinberg, S. J., and Fox Iii, L. 2009. Identifying Dicymbe corymbosa monodominant forests in Guyana using satellite imagery. *Biotropica*, 41, 7–15.

Dennison, P. E., Roberts, D. A., and Peterson, S. H. 2007. Spectral shape-based temporal compositing algorithms for MODIS surface reflectance data. *Remote Sensing of Environment*, 109, 510–522.

Desclee, B., Simonetti, D., Mayaux, P., and Achard, F. 2013. Multi-sensor monitoring system for forest cover change assessment in Central Africa. *IEEE Journal on Selected Topics in Applied Earth Observations and Remote Sensing*, 6, 110–120.

Doughty, C. E. and Goulden, M. L. 2008. Seasonal patterns of tropical forest leaf area index and CO2 exchange. *Journal of Geophysical Research: Biogeosciences* (2005–2012), 113.

Dubreuil, V., Debortoli, N., Funatsu, B., Nédélec, V., and Durieux, L. 2012. Impact of land-cover change in the Southern Amazonia climate: A case study for the region of Alta Floresta, Mato Grosso, Brazil. *Environmental Monitoring and Assessment*, 184, 877–891.

Duveiller, G., Defourny, P., Desclée, B., and Mayaux, P. 2008. Deforestation in Central Africa: Estimates at regional, national and landscape levels by advanced processing of systematically-distributed Landsat extracts. *Remote Sensing of Environment*, 112, 1969–1981.

Elumnoh, A. and Shrestha, R. P. 2000. Application of DEM data to Landsat image classification: Evaluation in a tropical wet-dry landscape of Thailand. *Photogrammetric Engineering and Remote Sensing*, 66, 297–304.

Emelyanova, I. V., McVicar, T. R., Van Niel, T. G., Li, L. T., and van Dijk, A. I. 2013. Assessing the accuracy of blending Landsat–MODIS surface reflectances in two landscapes with contrasting spatial and temporal dynamics: A framework for algorithm selection. *Remote Sensing of Environment*, 133, 193–209.

Faber-Langendoen, D., Keeler-Wolf, T., Meidinger, D., Josse, C., Weakley, A., Tart, D., Navarro, G. et al. 2012. *Classification and Description of World Formation Types*: Hierarchy Revisions Working Group, Federal Geographic Data Committee, FGDC Secretariat, US Geological Survey. Reston, VA, and NatureServe, Arlington, VA.

Ferry, B., Morneau, F., Bontemps, J. D., Blanc, L., and Freycon, V. 2010. Higher treefall rates on slopes and waterlogged soils result in lower stand biomass and productivity in a tropical rain forest. *Journal of Ecology*, 98, 106–116.

Fisher, A. 2014. Cloud and cloud-shadow detection in SPOT5 HRG satellite imagery with automated morphological feature extraction. *Remote Sensing*, 6, 776–800.

Flood, N. 2013. Seasonal composite Landsat TM/ETM+ images using the Medoid (a Multi-Dimensional Median). *Remote Sensing*, 5, 6481–6500.

Foody, G. M. and Hill, R. 1996. Classification of tropical forest classes from Landsat TM data. *International Journal of Remote Sensing*, 17, 2353–2367.

Foody, G. M., Palubinskas, G., Lucas, R. M., Curran, P. J., and Honzak, M. 1996. Identifying terrestrial carbon sinks: Classification of successional stages in regenerating tropical forest from Landsat TM data. *Remote Sensing of Environment*, 55, 205–216.

Foody, G. M. and Cutler, M. E. 2003. Tree biodiversity in protected and logged Bornean tropical rain forests and its measurement by satellite remote sensing. *Journal of Biogeography*, 30, 1053–1066.

Friedl, M. A., McIver, D. K., Hodges, J. C., Zhang, X., Muchoney, D., Strahler, A. H., Woodcock, C. E. et al. 2002. Global land cover mapping from MODIS: Algorithms and early results. *Remote Sensing of Environment*, 83, 287–302.

Friedl, M. A., Sulla-Menashe, D., Tan, B., Schneider, A., Ramankutty, N., Sibley, A., and Huang, X. 2010. MODIS Collection 5 global land cover: Algorithm refinements and characterization of new datasets. *Remote Sensing of Environment*, 114, 168–182.

Gao, B.-C. 1996. NDWI—A normalized difference water index for remote sensing of vegetation liquid water from space. *Remote Sensing of Environment*, 58, 257–266.

Gao, F., Masek, J. G., Schwaller, M., and Hall, F. 2006. On the blending of the Landsat and MODIS surface reflectance: Predicting daily Landsat. *IEEE Transactions on Geoscience and Remote Sensing*, 44, 2207–2208.

Garzon-Lopez, C. X., Bohlman, S. A., Olff, H., and Jansen, P. A. 2013. Mapping tropical forest trees using High-resolution aerial digital photographs. *Biotropica*, 45, 308–316.

Gentry, A. H. 1988. Tree species richness of upper Amazonian forests. *Proceedings of the National Academy of Sciences*, 85, 156–159.

Gibbes, C., Adhikari, S., Rostant, L., Southworth, J., and Qiu, Y. 2010. Application of object based classification and high resolution satellite imagery for savanna ecosystem analysis. *Remote Sensing*, 2, 2748–2772.

Gibson, L., Lee, T. M., Koh, L. P., Brook, B. W., Gardner, T. A., Barlow, J., Peres, C. A. et al. 2011. Primary forests are irreplaceable for sustaining tropical biodiversity. *Nature*, 478, 378–381.

Givnish, T. J. 1999. On the causes of gradients in tropical tree diversity. *Journal of Ecology*, 87, 193–210.

Gond, V., Bartholomé, E., Ouattara, F., Nonguierma, A., and Bado, L. 2004. Surveillance et cartographie des plans d'eau et des zones humides et inondables en régions arides avec l'instrument VEGETATION embarqué sur SPOT-4. *International Journal of Remote Sensing*, 25, 987–1004.

Gond, V. and Guitet, S. 2009. Elaboration d'un diagnostic post-exploitation par télédétection spatiale pour la gestion des forêts de Guyane. *Bois et Forêts des Tropiques*, 299, 5–13.

Gond, V., Freycon, V., Molino, J.-F., Brunaux, O., Ingrassia, F., Joubert, P., Pekel, J.-F. et al. 2011. Broad-scale spatial pattern of forest landscape types in the Guiana Shield. *International Journal of Applied Earth Observation and Geoinformation*, 13, 357–367.

Gond, V., Fayolle, A., Pennec, A., Cornu, G., Mayaux, P., Camberlin, P., Doumenge, C. et al. 2013. Vegetation structure and greenness in Central Africa from Modis multi-temporal data. *Philosophical Transactions of the Royal Society B: Biological Sciences*, 368.

González-Orozco, C. E., Mulligan, M., Trichon, V., and Jarvis, A. 2010. Taxonomic identification of Amazonian tree crowns from aerial photography. *Applied Vegetation Science*, 13, 510–519.

Goodwin, N. R., Collett, L. J., Denham, R. J., Flood, N., and Tindall, D. 2013. Cloud and cloud shadow screening across Queensland, Australia: An automated method for Landsat TM/ETM+ time series. *Remote Sensing of Environment*, 134, 50–65.

Goodwin, N. R. and Collett, L. J. 2014. Development of an automated method for mapping fire history captured in Landsat TM and ETM+ time series across Queensland, Australia. *Remote Sensing of Environment*, 148, 206–221.

Göttlicher, D., Obregón, A., Homeier, J., Rollenbeck, R., Nauss, T., and Bendix, J. 2009. Land-cover classification in the Andes of southern Ecuador using Landsat ETM+ data as a basis for SVAT modelling. *International Journal of Remote Sensing*, 30, 1867–1886.

AQ19 Griffiths, P., Kuemmerle, T., Baumann, M., Radeloff, V. C., Abrudan, I. V., Lieskovsky, J., Munteanu, C. et al. 2013. Forest disturbances, forest recovery, and changes in forest types across the Carpathian ecoregion from 1985 to 2010 based on Landsat image composites. *Remote Sensing of Environment*.

Hansen, M. C., Roy, D. P., Lindquist, E., Adusei, B., Justice, C. O., and Altstatt, A. 2008. A method for integrating MODIS and Landsat data for systematic monitoring of forest cover and change in the Congo Basin. *Remote Sensing of Environment*, 112, 2495–2513.

Helmer, E. and Ruefenacht, B. 2005. Cloud-free satellite image mosaics with regression trees and histogram matching. *Photogrammetric Engineering and Remote Sensing*, 71, 1079.

Helmer, E. and Lefsky, M. 2006. Forest canopy heights in Amazon River basin forests as estimated with the Geoscience Laser Altimeter System (GLAS), in *Monitoring Science and Technology Symposium: Unifying Knowledge for Sustainability in the Western Hemisphere*, September 21–25, 2004, C. Aguirre-Bravo, Pellicane, P. J., Burns, D. P., and Draggan, S. (eds.) Denver, CO: Proceedings RMRS-P-37CD/Ogden, UT: U.S. Department of Agriculture, Forest Service, Rocky Mountain Research Station, CD-ROM, pp. 802–808.

Helmer, E. and Ruefenacht, B. 2007a. A comparison of radiometric normalization methods when filling cloud gaps in Landsat imagery. *Canadian Journal of Remote Sensing*, 33, 325–340.

Helmer, E., Ruzycki, T. S., Wunderle, J. M., Vogesser, S., Ruefenacht, B., Kwit, C., Brandeis, T. J. et al. 2010. Mapping tropical dry forest height, foliage height profiles and disturbance type and age with a time series of cloud-cleared Landsat and ALI image mosaics to characterize avian habitat. *Remote Sensing of Environment*, 114, 2457–2473.

Helmer, E. H., Brown, S., and Cohen, W. 2000. Mapping montane tropical forest successional stage and land use with multi-date Landsat imagery. *International Journal of Remote Sensing*, 21, 2163–2183.

Helmer, E. H., Ramos, O., López, T. del. M., Quiñones, M., and Diaz, W. 2002. Mapping forest type and land cover of Puerto Rico, a component of the Caribbean biodiversity hotspot. *Caribbean Journal of Science*, 38, 165–183.

Helmer, E. H. and Ruefenacht, B. 2007b. A comparison of radiometric normalization methods when filling cloud gaps in Landsat imagery. *Canadian Journal of Remote Sensing/ Journal Canadien de Teledetection*, 33, 325–340.

Helmer, E. H., Kennaway, T. A., Pedreros, D. H., Clark, M. L., Marcano-Vega, H., Tieszen, L. L., Ruzycki, T. R. et al. 2008. Land cover and forest formation distributions for St. Kitts, Nevis, St. Eustatius, Grenada and Barbados from decision tree classification of cloud-cleared satellite imagery. *Caribbean Journal of Science*, 44, 175–198.

Helmer, E. H., Lefsky, M. A., and Roberts, D. A. 2009. Biomass accumulation rates of Amazonian secondary forest and biomass of old-growth forests from Landsat time series and the Geoscience Laser Altimeter System. *Journal of Applied Remote Sensing*, 3, 033505–033531.

Helmer, E. H., Ruzycki, T. S., Benner, J., Voggesser, S. M., Scobie, B. P., Park, C., Fanning, D. W. et al. 2012. Detailed maps of tropical forest types are within reach: Forest tree communities for Trinidad and Tobago mapped with multiseason Landsat and multiseason fine-resolution imagery. *Forest Ecology and Management*, 279, 147–166.

Hernández-Stefanoni, J. L., Alberto Gallardo-Cruz, J., Meave, J. A., and Dupuy, J. M. 2011. Combining geostatistical models and remotely sensed data to improve tropical tree richness mapping. *Ecological Indicators*, 11, 1046–1056.

AQ20 Hilker, T., Lyapustin, A. I., Tucker, C. J., Sellers, P. J., Hall, F. G., and Wang, Y. 2012. Remote sensing of tropical ecosystems: Atmospheric correction and cloud masking matter. *Remote Sensing of Environment*, 127, 370–384.

Holben, B. N. 1986. Characteristics of maximum-value composite images from temporal AVHRR data. *International Journal of Remote Sensing*, 7, 1417–1434.

Holdridge, L. R. 1967. *Life Zone Ecology*. San José, CA: Tropical Science Center.

Houghton, R. A. 2013. The emissions of carbon from deforestation and degradation in the tropics: Past trends and future potential. *Carbon Management*, 4, 539–546.

Huang, C., Wylie, B., Homer, C., Yang, L., and Zylstra, G. 2002. Derivation of a Tasseled Cap transformation based on Landsat 7 at-satellite reflectance. *International Journal of Remote Sensing*, 23, 1741–1748.

Huang, C., Thomas, N., Goward, S. N., Masek, J. G., Zhu, Z., Townshend, J. R., and Vogelmann, J. E. 2010. Automated masking of cloud and cloud shadow for forest change analysis using Landsat images. *International Journal of Remote Sensing*, 31, 5449–5464.

Huete, A. R. 1988. A soil-adjusted vegetation index (SAVI). *Remote Sensing of Environment*, 25, 295–309.

IPCC. 2006. *IPCC Guidelines for National Greenhouse Gas Inventories*. Hayama, Japan: Global Environmental Strategies (IGES).

AQ21 IPCC. 2014. *Climate Change 2014: Mitigation of Climate Change, Contribution of Working Group III to the Fifth Assessment Report of the Intergovernmental Panel on Climate Change*, O. Edenhofer, Pichs-Madruga, R., Sokona, Y., Farahani, E., Kadner, S., Seyboth, K., Adler, A. et al. (eds.). Cambridge, U.K./New York: Cambridge University Press.

Irish, R. R., Barker, J. L., Goward, S. N., and Arvidson, T. 2006. Characterization of the Landsat-7 ETM+ automated cloud-cover assessment (ACCA) algorithm. *Photogrammetric Engineering and Remote Sensing*, 72, 1179.

Joshi, P. K. K., Roy, P. S., Singh, S., Agrawal, S., and Yadav, D. 2006. Vegetation cover mapping in India using multi-temporal IRS Wide Field Sensor (WiFS) data. *Remote Sensing of Environment*, 103, 190–202.

Joubert, P., Bourgeois, U., Linarés, S., Gond, V., Verger, G., Allo, S., and Coppel, A. 2012. L'observatoire de l'activité minière, un outil adapté à la surveillance de l'environnement, in *XV° symposium de la Société Savante Latino-Américaine de Télédétection et des Systèmes d'Informations Spatiales (SELPER)*. Cayenne, France.

Kennaway, T. and Helmer, E. 2007. The forest types and ages cleared for land development in Puerto Rico. *GIScience & Remote Sensing*, 44, 356–382.

Kennaway, T. A., Helmer, E. H., Lefsky, M. A., Brandeis, T. A., and Sherrill, K. R. 2008. Mapping land cover and estimating forest structure using satellite imagery and coarse resolution lidar in the Virgin Islands. *Journal of Applied Remote Sensing*, 2, 023551–023551–023527.

Langner, A., Hirata, Y., Saito, H., Sokh, H., Leng, C., Pak, C., and Raši, R. 2014. Spectral normalization of SPOT 4 data to adjust for changing leaf phenology within seasonal forests in Cambodia. *Remote Sensing of Environment*, 143, 122–130.

Laporte, N. T., Stabach, J. A., Grosch, R., Lin, T. S., and Goetz, S. J. 2007. Expansion of industrial logging in Central Africa. *Science*, 316, 1451–1451.

Laumonier, Y., Edin, A., Kanninen, M., and Munandar, A. W. 2010. Landscape-scale variation in the structure and biomass of the hill dipterocarp forest of Sumatra: Implications for carbon stock assessments. *Forest Ecology and Management*, 259, 505–513.

Laurance, W. F., Goosem, M., and Laurance, S. G. 2009. Impacts of roads and linear clearings on tropical forests. *Trends in Ecology & Evolution*, 24, 659–669.

Le Hégarat-Mascle, S. and André, C. 2009. Use of Markov random fields for automatic cloud/shadow detection on high resolution optical images. *ISPRS Journal of Photogrammetry and Remote Sensing*, 64, 351–366.

Lefsky, M. A. 2010. A global forest canopy height map from the moderate resolution imaging spectroradiometer and the geoscience laser altimeter system. *Geophysical Research Letters*, 37.

Lewis, S. L., Brando, P. M., Phillips, O. L., van der Heijden, G. M., and Nepstad, D. 2011. The 2010 amazon drought. *Science*, 331, 554–554.

Li, A., Huang, C., Sun, G., Shi, H., Toney, C., Zhu, Z., Rollins, M. G. et al. 2011. Modeling the height of young forests regenerating from recent disturbances in Mississippi using Landsat and ICESat data. *Remote Sensing of Environment*, 115, 1837–1849.

Loveland, T. and Belward, A. 1997. The IGBP-DIS global 1km land cover data set, DISCover: First results. *International Journal of Remote Sensing*, 18, 3289–3295.

Lu, D. 2005. Aboveground biomass estimation using Landsat TM data in the Brazilian Amazon. *International Journal of Remote Sensing*, 26, 2509–2525.

Lucas, R. M., Xiao, X., Hagen, S., and Frolking, S. 2002. Evaluating TERRA-1 MODIS data for discrimination of tropical secondary forest regeneration stages in the Brazilian Legal Amazon. *Geophysical Research Letters*, 29, 42-41–42-44.

Luo, Y., Trishchenko, A. P., and Khlopenkov, K. V. 2008. Developing clear-sky, cloud and cloud shadow mask for producing clear-sky composites at 250-meter spatial resolution for the seven MODIS land bands over Canada and North America. *Remote Sensing of Environment*, 112, 4167–4185.

Lyapustin, A., Wang, Y., and Frey, R. 2008. An automatic cloud mask algorithm based on time series of MODIS measurements. *Journal of Geophysical Research: Atmospheres (1984–2012)*, 113.

Malhi, Y., Wood, D., Baker, T. R., Wright, J., Phillips, O. L., Cochrane, T., Meir, P. et al. 2006. The regional variation of aboveground live biomass in old-growth Amazonian forests. *Global Change Biology*, 12, 1107–1138.

Malhi, Y. and Román-Cuesta, R. M. 2008. Analysis of lacunarity and scales of spatial homogeneity in IKONOS images of Amazonian tropical forest canopies. *Remote Sensing of Environment*, 112, 2074–2087.

Martinuzzi, S., Gould, W. A., and González, O. M. R. 2007. Creating cloud-free Landsat ETM+ data sets in tropical landscapes: Cloud and cloud-shadow removal. F. S. US Department of Agriculture (ed.), San Juan, PR: International Institute of Tropical Forestry.

Martinuzzi, S., Gould, W. A., Ramos González, O. M., Martínez Robles, A., Calle Maldonado, P., Pérez-Buitrago, N., and Fumero Caban, J. J. 2008. Mapping tropical dry forest habitats integrating Landsat NDVI, Ikonos imagery, and topographic information in the Caribbean Island of Mona. *Revista de Biologia Tropical*, 56, 625–639.

Mayaux, P., Achard, F., and Malingreau, J.-P. 1998. Global tropical forest area measurements derived from coarse resolution satellite imagery: A comparison with other approaches. *Environmental Conservation*, 25, 37–52.

Mayaux, P., Bartholomé, E., Fritz, S., and Belward, A. 2004. A new land-cover map of Africa for the year 2000. *Journal of Biogeography*, 31, 861–877.

Mayaux, P., Pekel, J.-F., Desclée, B., Donnay, F., Lupi, A., Achard, F., Clerici, M. et al. 2013. State and evolution of the African rainforests between 1990 and 2010. *Philosophical Transactions of the Royal Society B: Biological Sciences*, 368.

McCallum, I., Obersteiner, M., Nilsson, S., and Shvidenko, A. 2006. A spatial comparison of four satellite derived 1 km global land cover datasets. *International Journal of Applied Earth Observation and Geoinformation*, 8, 246–255.

Miller, S. D., Goulden, M. L., Hutyra, L. R., Keller, M., Saleska, S. R., Wofsy, S. C., Figueira, A. M. S. et al. 2011. Reduced impact logging minimally alters tropical rainforest carbon and energy exchange. *Proceedings of the National Academy of Sciences*, 108, 19431–19435.

Mitchard, E. T. A., Feldpausch, T. R., Brienen, R. J. W., Lopez-Gonzalez, G., Monteagudo, A., Baker, T. R., Lewis, S. L. et al. 2014. Markedly divergent estimates of Amazon forest carbon density from ground plots and satellites. *Global Ecology and Biogeography*, 23, 935–946.

Morton, D. C., DeFries, R. S., Nagol, J., Souza Jr., C. M., Kasischke, E. S., Hurtt, G. C., and Dubayah, R. 2011. Mapping canopy damage from understory fires in Amazon forests using annual time series of Landsat and MODIS data. *Remote Sensing of Environment*, 115, 1706–1720.

Morton, D. C., Nagol, J., Carabajal, C. C., Rosette, J., Palace, M., Cook, B. D., Vermote, E. F. et al. 2014. Amazon forests maintain consistent canopy structure and greenness during the dry season. *Nature*, 506, 221–224.

Myneni, R. B., Yang, W., Nemani, R. R., Huete, A. R., Dickinson, R. E., Knyazikhin, Y., Didan, K. et al. 2007. Large seasonal swings in leaf area of Amazon rainforests. *Proceedings of the National Academy of Sciences*, 104, 4820–4823.

Nagendra, H. and Rocchini, D. 2008. High resolution satellite imagery for tropical biodiversity studies: The devil is in the detail. *Biodiversity and Conservation*, 17, 3431–3442.

Nagendra, H., Rocchini, D., Ghate, R., Sharma, B., and Pareeth, S. 2010. Assessing plant diversity in a dry tropical forest: Comparing the utility of Landsat and IKONOS satellite images. *Remote Sensing*, 2, 478–496.

Nelson, R. F., Kimes, D. S., Salas, W. A., and Routhier, M. 2000. Secondary forest age and tropical forest biomass estimation using Thematic Mapper imagery: Single-year tropical forest age classes, a surrogate for standing biomass, cannot be reliably identified using single-date tm imagery. *Bioscience*, 50, 419–431.

Nemani, R. R., Keeling, C. D., Hashimoto, H., Jolly, W. M., Piper, S. C., Tucker, C. J., Myneni, R. B. et al. 2003. Climate-driven increases in global terrestrial net primary production from 1982 to 1999. *Science*, 300, 1560–1563.

Newman, M. E., McLaren, K. P., and Wilson, B. S. 2011. Comparing the effects of classification techniques on landscape-level assessments: Pixel-based versus object-based classification. *International Journal of Remote Sensing*, 32, 4055–4073.

Omeja, P. A., Obua, J., Rwetsiba, A., and Chapman, C. A. 2012. Biomass accumulation in tropical lands with different disturbance histories: Contrasts within one landscape and across regions. *Forest Ecology and Management*, 269, 293–300.

Oreopoulos, L., Wilson, M. J., and Várnai, T. 2011. Implementation on Landsat data of a simple cloud-mask algorithm developed for MODIS land bands. *IEEE Geoscience and Remote Sensing Letters*, 8, 597–601.

Oza, M., Srivastava, V., and Devaiah, P. 1996. Estimating tree volume in tropical dry deciduous forest from Landsat TM data. *Geocarto International*, 11, 33–39.

Palace, M., Keller, M., Asner, G. P., Hagen, S., and Braswell, B. 2008. Amazon forest structure from IKONOS satellite data and the automated characterization of forest canopy properties. *Biotropica*, 40, 141–150.

Park, S. 2009. Synchronicity between satellite-measured leaf phenology and rainfall regimes in tropical forests. *Photogrammetric Engineering and Remote Sensing*, 75, 1231–1237.

Parker, C., Mitchell, A., Trivedi, M., Mardas, N., and Sosis, K. 2009. The little REDD+ book. *Global Canopy Foundation*, 132.

Parmesan, C. and Yohe, G. 2003. A globally coherent fingerprint of climate change impacts across natural systems. *Nature*, 421, 37–42.

AQ22 Partners, A. D. 2013. Approved VCS Methodology VM0007, Version 1.4, REDD Methodology Modules (REDD-MF), in *Sectoral Scope 14*, T. a. W. (ed.). International: Verified Carbon Standard.

Pennec, A., Gond, V., and Sabatier, D. 2011. Tropical forest phenology in French Guiana from MODIS time series. *Remote Sensing Letters*, 2, 337–345.

Peterson, G. D. and Heemskerk, M. 2001. Deforestation and forest regeneration following small-scale gold mining in the Amazon: The case of Suriname. *Environmental Conservation*, 28, 117–126.

Pflugmacher, D., Cohen, W. B., and E Kennedy, R. 2012. Using Landsat-derived disturbance history (1972–2010) to predict current forest structure. *Remote Sensing of Environment*, 122, 146–165.

Phillips, O. L., Aragão, L. E., Lewis, S. L., Fisher, J. B., Lloyd, J., López-González, G., Malhi, Y. et al. 2009. Drought sensitivity of the Amazon rainforest. *Science*, 323, 1344–1347.

Pinard, M. A. and Putz, F. E. 1996. Retaining forest biomass by reducing logging damage. *Biotropica*, 28(3), 278–295.

Pinty, B. and Verstraete, M. 1992. GEMI: A non-linear index to monitor global vegetation from satellites. *Vegetatio*, 101, 15–20.

Pithon, S., Jubelin, G., Guitet, S., and Gond, V. 2013. A statistical method for detecting logging-related canopy gaps using high-resolution optical remote sensing. *International Journal of Remote Sensing*, 34, 700–711.

Ploton, P., Pélissier, R., Proisy, C., Flavenot, T., Barbier, N., Rai, S. N., and Couteron, P. 2011. Assessing aboveground tropical forest biomass using Google Earth canopy images. *Ecological Applications*, 22, 993–1003.

Portillo-Quintero, C. A. and Sánchez-Azofeifa, G. A. 2010. Extent and conservation of tropical dry forests in the Americas. *Biological Conservation*, 143, 144–155.

Pringle, M., Schmidt, M., and Muir, J. 2009. Geostatistical interpolation of SLC-off Landsat ETM+ images. *ISPRS Journal of Photogrammetry and Remote Sensing*, 64, 654–664.

Qi, J., Chehbouni, A., Huete, A., Kerr, Y., and Sorooshian, S. 1994. A modified soil adjusted vegetation index. *Remote Sensing of Environment*, 48, 119–126.

Roberts, D., Numata, I., Holmes, K., Batista, G., Krug, T., Monteiro, A., Powell, B. et al. 2002. Large area mapping of land-cover change in Rondônia using multitemporal spectral mixture analysis and decision tree classifiers. *Journal of Geophysical Research*, 107, 8073.

Rouse, J., Haas, R., Schell, J., Deering, D., and Harlan, J. 1974. *Monitoring the Vernal Advancement and Retrogradation (Greenwave Effect) of Natural Vegetation*. College Station, TX: Texas A & M University, Remote Sensing Center.

Roy, D. P., Ju, J., Lewis, P., Schaaf, C., Gao, F., Hansen, M., and Lindquist, E. 2008. Multi-temporal MODIS-Landsat data fusion for relative radiometric normalization, gap filling, and prediction of Landsat data. *Remote Sensing of Environment*, 112, 3112–3130.

Roy, D. P., Ju, J., Kline, K., Scaramuzza, P. L., Kovalskyy, V., Hansen, M., Loveland, T. R. et al. 2010. Web-enabled Landsat Data (WELD): Landsat ETM+ composited mosaics of the conterminous United States. *Remote Sensing of Environment*, 114, 35–49.

Saatchi, S., Houghton, R., Dos Santos Alvala, R., Soares, J., and Yu, Y. 2007. Distribution of aboveground live biomass in the Amazon basin. *Global Change Biology*, 13, 816–837.

Saatchi, S. S., Harris, N. L., Brown, S., Lefsky, M., Mitchard, E. T., Salas, W., Zutta, B. R. et al. 2011. Benchmark map of forest carbon stocks in tropical regions across three continents. *Proceedings of the National Academy of Sciences*, 108, 9899–9904.

Salimon, C. I., Putz, F. E., Menezes-Filho, L., Anderson, A., Silveira, M., Brown, I. F., and Oliveira, L. 2011. Estimating state-wide biomass carbon stocks for a REDD plan in Acre, Brazil. *Forest Ecology and Management*, 262, 555–560.

Salk, C. F., Chazdon, R., and Andersson, K. 2013. Detecting landscape-level changes in tree biomass and biodiversity: Methodological constraints and challenges of plot-based approaches. *Canadian Journal of Forest Research*, 43, 799–808.

Salovaara, K. J., Thessler, S., Malik, R. N., and Tuomisto, H. 2005. Classification of Amazonian primary rain forest vegetation using Landsat ETM+ satellite imagery. *Remote Sensing of Environment*, 97, 39–51.

Samanta, A., Ganguly, S., Hashimoto, H., Devadiga, S., Vermote, E., Knyazikhin, Y., Nemani, R. R. et al. 2010. Amazon forests did not green-up during the 2005 drought. *Geophysical Research Letters*, 37.

Sánchez-Azofeifa, A., Rivard, B., Wright, J., Feng, J.-L., Li, P., Chong, M. M., and Bohlman, S. A. 2011. Estimation of the distribution of Tabebuia guayacan (Bignoniaceae) using high-resolution remote sensing imagery. *Sensors*, 11, 3831–3851.

Scaramuzza, P. L., Bouchard, M. A., and Dwyer, J. L. 2012. Development of the Landsat data continuity mission cloud-cover assessment algorithms. *IEEE Transactions on Geoscience and Remote Sensing*, 50, 1140–1154.

Sesnie, S. E., Gessler, P. E., Finegan, B., and Thessler, S. 2008. Integrating Landsat TM and SRTM-DEM derived variables with decision trees for habitat classification and change detection in complex neotropical environments. *Remote Sensing of Environment*, 112, 2145–2159.

Sesnie, S. E., Finegan, B., Gessler, P. E., Thessler, S., Bendana, Z. R., and Smith, A. M. 2010. The multispectral separability of Costa Rican rainforest types with support vector machines and Random Forest decision trees. *International Journal of Remote Sensing*, 31, 2885–2909.

Siegert, F., Ruecker, G., Hinrichs, A., and Hoffmann, A. 2001. Increased damage from fires in logged forests during droughts caused by El Nino. *Nature*, 414, 437–440.

Sist, P. and Ferreira, F. N. 2007. Sustainability of reduced-impact logging in the Eastern Amazon. *Forest Ecology and Management*, 243, 199–209.

Skidmore, A. K. 1989. An expert system classifies eucalypt forest types using thematic mapper data and a digital terrain model. *Photogrammetric Engineering and Remote Sensing*, 55, 1449–1464.

Skole, D. and Tucker, C. 1993. Tropical deforestation and habitat fragmentation in the Amazon: Satellite data from 1978 to 1988. *Science*, 260, 1905–1910.

Small, C. 2004. The Landsat ETM+ spectral mixing space. *Remote Sensing of Environment*, 93, 1–17.

Song, C. 2013. Optical remote sensing of forest leaf area index and biomass. *Progress in Physical Geography*, 37, 98–113.

Souza Jr., C. and Barreto, P. 2000. An alternative approach for detecting and monitoring selectively logged forests in the Amazon. *International Journal of Remote Sensing*, 21, 173–179.

Souza Jr., C., Firestone, L., Silva, L. M., and Roberts, D. 2003. Mapping forest degradation in the Eastern Amazon from SPOT 4 through spectral mixture models. *Remote Sensing of Environment*, 87, 494–506.

Souza Jr., C. M., Roberts, D. A., and Cochrane, M. A. 2005. Combining spectral and spatial information to map canopy damage from selective logging and forest fires. *Remote Sensing of Environment*, 98, 329–343.

Souza Jr., C. M., Siqueira, J. V., Sales, M. H., Fonseca, A. V., Ribeiro, J. G., Numata, I., Cochrane, M. A. et al. 2013. Ten-year Landsat classification of deforestation and forest degradation in the Brazilian Amazon. *Remote Sensing*, 5, 5493–5513.

AQ23 Souza Jr., C. M. and Siqueira, J. V. N. 2013. ImgTools: A software for optical remotely sensed data analysis, in *Anais XVI Simpósio Brasileiro de Sensoriamento Remoto - SBSR. I. N. d. P. E. (INPE)*. Foz do Iguaçu, Brazil: Instituto Nacional de Pesquisas Espaciais (INPE), pp. 1571–1578 .

Steininger, M. 2000. Satellite estimation of tropical secondary forest above-ground biomass: Data from Brazil and Bolivia. *International Journal of Remote Sensing*, 21, 1139–1157.

Stephens, B. B., Gurney, K. R., Tans, P. P., Sweeney, C., Peters, W., Bruhwiler, L., Ciais, P. et al. 2007. Weak northern and strong tropical land carbon uptake from vertical profiles of atmospheric CO2. *Science*, 316, 1732–1735.

AQ24 Strabala, K. I. 2005. MODIS cloud mask user's guide. , C. I. f. M. S. Studies (ed.). Madison, WI: University of Wisconsin–Madison, pp. 32.

Thenkabail, P. S., Hall, J., Lin, T., Ashton, M. S., Harris, D., and Enclona, E. A. 2003. Detecting floristic structure and pattern across topographic and moisture gradients in a mixed species Central African forest using IKONOS and Landsat-7 ETM+ images. *International Journal of Applied Earth Observation and Geoinformation*, 4, 255–270.

Thenkabail, P. S., Enclona, E. A., Ashton, M. S., Legg, C., and De Dieu, M. J. 2004. Hyperion, IKONOS, ALI, and ETM+ sensors in the study of African rainforests. *Remote Sensing of Environment*, 90, 23–43.

Thessler, S., Ruokolainen, K., Tuomisto, H., and Tomppo, E. 2005. Mapping gradual landscape-scale floristic changes in Amazonian primary rain forests by combining ordination and remote sensing. *Global Ecology and Biogeography*, 14, 315–325.

Thessler, S., Sesnie, S., Ramos Bendaña, Z. S., Ruokolainen, K., Tomppo, E., and Finegan, B. 2008. Using k-nn and discriminant analyses to classify rain forest types in a Landsat TM image over northern Costa Rica. *Remote Sensing of Environment*, 112, 2485–2494.

Tickle, P., Lee, A., Lucas, R. M., Austin, J., and Witte, C. 2006. Quantifying Australian forest floristics and structure using small footprint LiDAR and large scale aerial photography. *Forest Ecology and Management*, 223, 379–394.

Tottrup, C. 2004. Improving tropical forest mapping using multi-date Landsat TM data and pre-classification image smoothing. *International Journal of Remote Sensing*, 25, 717–730.

Tottrup, C., Rasmussen, M., Samek, J., and Skole, D. 2007. Towards a generic approach for characterizing and mapping tropical secondary forests in the highlands of mainland Southeast Asia. *International Journal of Remote Sensing*, 28, 1263–1284.

Townshend, J., Justice, C., Li, W., Gurney, C., and McManus, J. 1991. Global land cover classification by remote sensing: Present capabilities and future possibilities. *Remote Sensing of Environment*, 35, 243–255.

Trichon, V. and Julien, M.-P. 2006. Tree species identification on large-scale aerial photographs in a tropical rain forest, French Guiana-application for management and conservation. *Forest Ecology and Management*, 225, 51–61.

Tucker, C. J., Goff, T., and Townshend, J. 1985. African land-cover classification using satellite data. *Science*, 227, 369–375.

Uhl, C. and Buschbacher, R. 1985. A disturbing synergism between cattle ranch burning practices and selective tree harvesting in the eastern Amazon. *Biotropica*, 17(4), 265–268.

USGS. 2003. *Preliminary Assessment of Landsat 7 ETM+ Data Following Scan Line Corrector Malfunction USGS*. Sioux Falls, SD: United States Geological Survey.

Vancutsem, C., Pekel, J.-F., Evrard, C., Malaisse, F., and Defourny, P. 2009. Mapping and characterizing the vegetation types of the Democratic Republic of Congo using SPOT VEGETATION time series. *International Journal of Applied Earth Observation and Geoinformation*, 11, 62–76.

Verhegghen, A., Mayaux, P., De Wasseige, C., and Defourny, P. 2012. Mapping Congo Basin vegetation types from 300 m and 1 km multi-sensor time series for carbon stocks and forest areas estimation. *Biogeosciences*, 9, 5061–5079.

Vickers, B., Trines, E., and Pohnan, E. 2012. Community guidelines for accessing forestry voluntary carbon markets. R. o. f. A. a. t. Pacific (eds.). Bangkok, Thailand: Food and Agriculture Organization of the United Nations, pp. 196.

Vieira, I. C. G., de Almeida, A. S., Davidson, E. A., Stone, T. A., Reis de Carvalho, C. J., and Guerrero, J. B. 2003. Classifying successional forests using Landsat spectral properties and ecological characteristics in eastern Amazonia. *Remote Sensing of Environment*, 87, 470–481.

Vitousek, P. M. 1994. Beyond global warming: Ecology and global change. *Ecology*, 75, 1861–1876.

Wang, B. 1999. Automated detection and removal of clouds and their shadows from Landstat TM images. *IEICE Transactions on Information and Systems*, 82, 453–460.

Wertz-Kanounnikoff, S. 2008. *Monitoring Forest Emissions, A Review of Methods*. Bogor, Indonesia: CIFOR.

Whiteside, T. G., Boggs, G. S., and Maier, S. W. 2011. Comparing object-based and pixel-based classifications for mapping savannas. *International Journal of Applied Earth Observation and Geoinformation*, 13, 884–893.

Wijaya, A., Liesenberg, V., and Gloaguen, R. 2010. Retrieval of forest attributes in complex successional forests of Central Indonesia: Modeling and estimation of bitemporal data. *Forest Ecology and Management*, 259, 2315–2326.

Wilson, E. O. 1988. The current state of biological diversity, in *Biodiversity*, E. O. Wilson and Peters, F. M. (eds.) Washington, DC: National Academy Press, pp. 3–18.

Wittmann, F., Anhuf, D., and Funk, W. J. 2002. Tree species distribution and community structure of central Amazonian várzea forests by remote-sensing techniques. *Journal of Tropical Ecology*, 18, 805–820.

Woods, P. 1989. Effects of logging, drought, and fire on structure and composition of tropical forests in Sabah, Malaysia. *Biotropica*, 21(4), 290–298.

Wulder, M. A., White, J. C., Nelson, R. F., Næsset, E., Ørka, H. O., Coops, N. C., Hilker, T. et al. 2012. Lidar sampling for large-area forest characterization: A review. *Remote Sensing of Environment*, 121, 196–209.

Xiao, X., Hagen, S., Zhang, Q., Keller, M., and Moore III, B. 2006. Detecting leaf phenology of seasonally moist tropical forests in South America with multi-temporal MODIS images. *Remote Sensing of Environment*, 103, 465–473.

Xu, X., Du, H., Zhou, G., Ge, H., Shi, Y., Zhou, Y., Fan, W. et al. 2011. Estimation of aboveground carbon stock of Moso bamboo (*Phyllostachys heterocycla* var. pubescens) forest with a Landsat Thematic Mapper image. *International Journal of Remote Sensing*, 32, 1431–1448.

Zelazowski, P., Malhi, Y., Huntingford, C., Sitch, S., and Fisher, J. B. 2011. Changes in the potential distribution of humid tropical forests on a warmer planet. *Philosophical Transactions of the Royal Society A: Mathematical, Physical and Engineering Sciences*, 369, 137–160.

Zhao, M. and Running, S. W. 2010. Drought-induced reduction in global terrestrial net primary production from 2000 through 2009. *Science*, 329, 940–943.

Zhu, X., Chen, J., Gao, F., Chen, X., and Masek, J. G. 2010. An enhanced spatial and temporal adaptive reflectance fusion model for complex heterogeneous regions. *Remote Sensing of Environment*, 114, 2610–2623.

Zhu, X., Gao, F., Liu, D., and Chen, J. 2012. A modified neighborhood similar pixel interpolator approach for removing thick clouds in Landsat images. *IEEE Geoscience and Remote Sensing Letters*, 9, 521–525.

Zhu, Z. and Woodcock, C. E. 2012. Object-based cloud and cloud shadow detection in Landsat imagery. *Remote Sensing of Environment*, 118, 83–94.

Zhu, Z., Woodcock, C. E., and Olofsson, P. 2012. Continuous monitoring of forest disturbance using all available Landsat imagery. *Remote Sensing of Environment*, 122, 75–91.